

# Enhancing and Interpreting Deep Learning for Sea Ice Charting using the AutoICE Benchmark

Sepideh Jalayer<sup>a</sup>, Samira Alkaee Taleghan<sup>b</sup>, Rafael Pires de Lima<sup>a</sup>, Behzad Vahedi<sup>a</sup>, Nick Hughes<sup>c</sup>, Farnoush Banaei-Kashani<sup>b</sup>, and Morteza Karimzadeh<sup>a,\*</sup>

<sup>a</sup> Department of Geography, University of Colorado Boulder, Boulder, CO 80309 USA

<sup>b</sup> Department of Computer Science & Engineering, University of Colorado Denver, Denver, CO, USA

<sup>c</sup> Norwegian Ice Service, Norwegian Meteorological Institute, Tromsø, Norway

\* Corresponding author: [karimzadeh@colorado.edu](mailto:karimzadeh@colorado.edu)

E-mail address: [Sepideh.Jalayer@colorado.edu](mailto:Sepideh.Jalayer@colorado.edu); [samira.alkaee@ucdenver.edu](mailto:samira.alkaee@ucdenver.edu), [rafaelaugusto.piresdelima@colorado.edu](mailto:rafaelaugusto.piresdelima@colorado.edu); [behzad@colorado.edu](mailto:behzad@colorado.edu); [nicholsh@met.no](mailto:nicholsh@met.no), [farnoush.banaei-kashani@ucdenver.edu](mailto:farnoush.banaei-kashani@ucdenver.edu), [karimzadeh@colorado.edu](mailto:karimzadeh@colorado.edu)

## ABSTRACT

Accurate mapping of sea ice is crucial for marine navigation and monitoring climate change. Automating sea ice mapping remains challenging due to remotely-sensed signal ambiguity, the dynamic nature of sea ice, and limited field measurements. The AutoICE challenge recently introduced a benchmark to advance deep learning for sea ice mapping. Top-performing solutions used the U-Net architecture with extra pre/post-processing steps and incorporated location features to obtain higher metrics. However, model interpretation and diagnostics remain limited. In this paper, we develop a customized multi-task DeepLabV3 model and achieve state-of-the-art performance of 87.3% combined score without extra pre- and post-processing, and outperform the current state of the art in predicting Stage of Development (SoD). Our approach enhances generalizability and outperforms current cross-scene sea ice retrieval methods. We further use interpretability methods including Gradient SHAP (Gradient Shapley Additive Explanations) and Gradient-Weighted Class Activation Mapping (Grad-CAM) to shed light on the contribution of individual input features and pixels on model decisions, including the role of geospatial (i.e., location) encoding. While incorporating geospatial encoding seemingly improves inference on the benchmark-designated test set, our additional model interpretation and spatial cross-validation reveal over-reliance on geolocation and overfitting to the test set. This suggests that the top-performing solutions on the AutoICE challenge are likely to lack geographic generalizability, a common issue in remote sensing, made worse by the use of location in the models. As such, we urge caution and recommend the use of spatial cross-validation and interpretability methods when using location information as input for remote sensing applications and further development of sea ice mapping algorithms.

**Keywords:** Sea ice mapping, convolutional neural networks (CNNs), geospatial encoding, feature importance, model generalizability.

## 1. Introduction

Sea ice plays a critical role in the Earth's climate system and regulates the ocean heat transfer and momentum flux (Gibson et al., 2020; Y. Huang et al., 2024; Meier et al., 2014). Further, with the declining trend of sea ice extent year over year, there is an increased interest in maritime navigation support in the Arctic with accurate and timely mapping of sea ice extent, concentration, and type (Wagner et al., 2020). Sea Ice Concentration (SIC) reflects the proportion of an area covered by ice. Stage of Development (SoD) or ice age, also known as ice type, is a proxy for ice thickness, posing varying levels of hazard to marine navigation, and having significance in climate and environmental studies. The third essential characteristic, floe Size (FLOE), identifies the size distribution of ice flakes and floes and helps determine the extent of ice fragmentation and the presence of leads. These parameters are currently mapped using manual techniques and image interpretation by expert ice analysts at ice services around the world. These operations are labor-intensive and time-consuming and have been the target of automation techniques since the 1980s (Key et al., 2014). Increased computational capacity, improved generations of satellite sensors and open access to data, and a renewal of the interest in AI approaches has led to an increased interest in automating sea ice mapping using space-borne sensors such as optical sensors, passive microwave radiometers, altimeters, synthetic aperture radar (SAR) (Lyu et al., 2022; Song et al., 2021; Wang and Li, 2021) and Global Navigation Satellite System-Reflectometry (GNSS-R) (Yan and Huang, 2016). Even though optical satellite images provide valuable information for distinguishing between sea ice and open water and some information on different ice types, they are unavailable under cloudy or dark conditions and are limited to thermal infrared (coarse resolution) at high latitudes during the winter polar night. However, SAR and passive microwave radiometers allow large-scale observations of sea ice year-round, since they can obtain images regardless of sunlight or cloud cover.

Recently, several studies have applied machine learning algorithms to map sea ice parameters (Andersson et al., 2021; Song et al., 2021). Earlier studies applied supervised algorithms including Support Vector Machines (SVM), Random Forests (RF), and

Decision Trees (DT) (Liu et al., 2015; Zhu et al., 2021). Deep learning algorithms, particularly convolutional neural networks (CNNs), have shown promising results in improving segmentation and classification performance owing to their ability to automatically learn hierarchical features, unlike traditional machine learning algorithms. Several CNN-based deep learning models have been proposed to classify or segment sea ice parameters, for SIC estimation (X. Chen et al., 2024c; De Gelis et al., 2021; Stokholm et al., 2022) binary ice-water classification (Pires De Lima and Karimzadeh, 2023), or multi-class sea ice classification (Huang et al., 2023; Khaleghian et al., 2021; Pires de Lima et al., 2023; Vahedi et al., 2024). Research in this area has primarily leveraged existing CNN architectures with minor modifications to tailor to sea ice mapping. However, performance still remains lower than expected for operational needs, especially for certain classes, like young ice or thin first year ice which are too frequently mistaken for water (Pires De Lima and Karimzadeh, 2023). Therefore, the resulting automated products that can facilitate both operational use and climate research are not yet reliable, and these automated models cannot be trusted or adopted by operational centers. In what follows, we identify the research challenges to close this gap, and our contributions to move in that direction.

All-sky SAR images in general, and the C-band (5.405 GHz) observations provided by Sentinel-1 in particular, are higher resolution than passive microwave, and capture more texture details of sea ice, which can be advantageous for discrimination and classification (Færch et al., 2024; W. Huang et al., 2024; Y. Huang et al., 2024; Qu et al., 2024). SAR has quickly become the primary data source for automated sea ice mapping efforts. For instance, the widely used Sentinel-1 Extra Wide mode provides cross-polarized (HV) and co-polarized (HH) observations over the Arctic Ocean. Each channel measures distinct information and has limited effectiveness in distinguishing between various ice types or surface features (Shokr and Dabboor, 2023). For sea ice, HH polarization typically captures the surface scattering (the dominant scattering mechanism of first year ice due to higher salinity), while the cross-polarized (HV) channel primarily provides information about volume scattering (the dominant scattering mechanism of multi-year ice due to air pockets) (Ye et al., 2023; Zhao et al., 2024). Previous research showed that HV polarization enhanced the ability to differentiate between sea ice and wind-roughened open water, as well as between deformed and level ice (Dierking, 2013; Pires de Lima et al., 2023). The dual-polarization (HH, HV) mode allows for better discrimination between different surface features and distinguish the sea ice characteristics (Færch et al., 2024; Shokr and Dabboor, 2023; Zhang et al., 2021). Given deep learning's black box nature, previous research has mainly quantified the *overall* deep learning performance using different sensors, such as SAR or passive microwave (X. Chen et al., 2024b, 2024a). However, research remains limited on the contribution of each SAR or passive microwave polarization or band in a deep learning framework, especially when used in combination, for mapping *specific* classes of sea ice parameters such as SIC, SoD, or FLOE. This is one of the gaps that we address in this paper.

One major challenge for automatically mapping sea ice parameters utilizing SAR data is the ambiguity and similar signatures of radar backscatter for different ice types under varied environmental conditions and incidence angles (W. Guo et al., 2022; Shokr and Dabboor, 2023; Zakhvatkina et al., 2019). For instance, in the presence of high winds, the backscattering signatures of certain ice types and open water (OW) are very close, which introduces additional complexities and uncertainty for creating accurate sea ice maps. As Ye et al. (Ye et al., 2023) observed, in summer or during melting events, ice types of MYI (multi-year ice) and FYI (first-year ice) have similar SAR backscatter signatures. Therefore, classification algorithms that solely rely on backscattering coefficients ( $\sigma^\circ$ ) will have challenges due to these uncertainties depending on wind speed and other conditions (Zakhvatkina et al., 2017). CNN-based methods partly alleviate this by leveraging spatial context and texture features more efficiently to complement the observation of a point with observations of surrounding areas (Boulze et al., 2020; Pires De Lima and Karimzadeh, 2023). Nevertheless, ambiguities remain, such as for distinguishing between various ice types, as well as between calm open water and smooth first-year ice or windy open water and young ice (or MYI) (Zakhvatkina et al., 2017).

In addition, there is a relative shortage of high-quality labeled datasets for training and evaluation of automated methods. This limitation is further aggravated by the imbalanced nature of training datasets, and can have an adverse effect on a model's ability to learn on the less frequent classes such as new ice or nilas that are short-lived. A sea ice analyst also sometimes faces the same ambiguities in interpreting SAR signals, in which case they may rely on secondary sources of data, or their general knowledge of the area under interpretation during that season. We take inspiration from this, and study the effectiveness and reliability of deep learning models when leveraging geospatial position to help with spectral observation disambiguation. We rigorously investigate the impact on the overall and per-class performance, and study the degree to which the deep learning model relies on observations versus location for disambiguation.

More importantly, cross-scene generalization (i.e., geographic generalization) remains a critical limitation in remote sensing of sea ice. Thus, we investigate the effect of incorporating latitude and longitude on the cross-scene generalizability of the model and compare our approach against state-of-the-art cross-scene sea ice retrieval.

The key contributions of our work are summarized as follows:

- We improve sea ice segmentation performance and efficiency using a customized end-to-end DeepLabV3 model without extra pre- and post-processing steps, and with fewer training iterations compared to the state of the art, achieving the highest reported F1 score for SoD on the benchmark test dataset.
- We improve model generalizability across geographic regions, outperforming state-of-the-art cross-scene sea ice retrieval.

- We compare the performance of different ensembling strategies for improving performance.
- We interpret the models using Gradient SHAP (Gradient Shapley Additive Explanations) to provide quantitative information on how much individual input features contribute to the model's predictions for each class. We also employ Gradient-Weighted Class Activation Mapping (Grad-CAM) to visualize the specific areas of an input scene that contribute most to the model's decisions for different targets. This comprehensive analysis advances the development of automated sea ice mapping techniques.
- We examine the impact of incorporating geospatial encoding (i.e., location) into deep learning for SIC estimation and classifying specific classes of SoD and FLOE. Our analysis demonstrates for which ice types location can help with signal disambiguation, and for which types it may lead to over-reliance on location, resulting in model memorization and overfitting.
- We conduct spatial cross-validation on the dataset and contrast the configurations and results against the AutoICE benchmark's designated cross-validation scheme, and provide practical recommendations for improved use of the dataset in developing automated sea ice charting methods. To the best of our knowledge, this is the first paper that conducts spatial cross-validation to examine the effect of incorporating geospatial encoding on the model performance and generalizability in other regions not covered by the dataset for sea ice characterization.

While our work provides an open-source end-to-end deep learning framework for automating the generation of sea ice charts, which provides value to the community, we believe that our interrogation of the deep learning model through interpretation methods provides a first-of-its-kind lens for the sea ice remote sensing community, through which the black box of deep learning is further unraveled. Through these analyses, we hope to make clear under which training configurations the scores resulting from deep learning methods can be potentially misleading, how to identify limitations of automated methods beyond scores, and based on the lessons learned, provide recommendations for adoption in operations as well as future research.

## 2. Dataset

The AutoICE Challenge published a labeled dataset along with a benchmark task to facilitate the development of automated sea ice mapping methods (Stokholm et al., 2024, Buus-Hinkler et al., 2022). It consists of 533 scenes from January 2018 to December 2021 which spread over the Canadian and Greenlandic Arctic. The 533 files (in NetCDF format, 513 training and 20 test scenes) contain Sentinel-1 Extra Wide Swath Mode (EW) C-band 5.405 GHz frequency Level 1 (HH and HV polarization, and incidence angle), a distance from land map for all Sentinel-1 pixels (Distance Map), Latitude and Longitude of subgrid points in the scene, AMSR2 brightness temperatures, numerical weather prediction (NWP) parameters from ERA5 Environmental Variables, and ice charts from the Canadian Ice Service (CIS) and DMI operational ice services. AMSR2 observations are resampled to Sentinel-1 spatial dimension at 50 by 50 (2 km) pixel resolution. Gaussian weighted interpolation is used for each vertical and horizontal polarization and radiance at 6.9, 7.3, 10.7, 18.7, 23.8, 36.5, and 89.0 GHz. ERA5 environmental variables, which include the 10m wind speed (eastward), the 10m wind speed (northward), 2m air temperature, skin temperature, total column water vapor, and total column cloud liquid water, are also resampled to Sentinel-1 geometry at 50 by 50 (2 kilometer) pixel resolution using Gaussian weighted interpolation (X. Chen et al., 2024b; Stokholm et al., 2024).

The dataset is available in two formats: a raw version and a ready-to-train version. For this study, we utilize the ready-to-train format, which includes preprocessed SAR images, distance maps, and ice charts, all resampled to 80 m pixel spacing (approximately 5000×5000 pixels). The scenes are normalized between -1 and 1, while polygon ice charts are assigned a value of 255 to indicate masked or invalid pixels. Any NaN values in the SAR scenes are replaced with 2. The SIC represents the percentage of an area covered by sea ice, ranging from 0% (open water) to 100% (fully covered sea ice). The SoD represents sea ice type (a proxy for ice thickness) which consists of 6 classes including open-water, new ice, young ice, thin first-year ice (thin FYI), thick first-year ice (thick FYI), and old ice. The floe size is a measure of the magnitude and continuity of the sea ice pieces or chunks, determined by 7 classes including open-water, cake ice (< 20 m), small floe (20 – 100 m), medium floe (100 – 500 m), big floe (500 m – 2 km), vast floe (> 2 km), and bergs, which include icebergs and glacier ice variants.

## 3. Geospatial Encoding and Input Variable Processing

### 3.1. Input Preprocessing

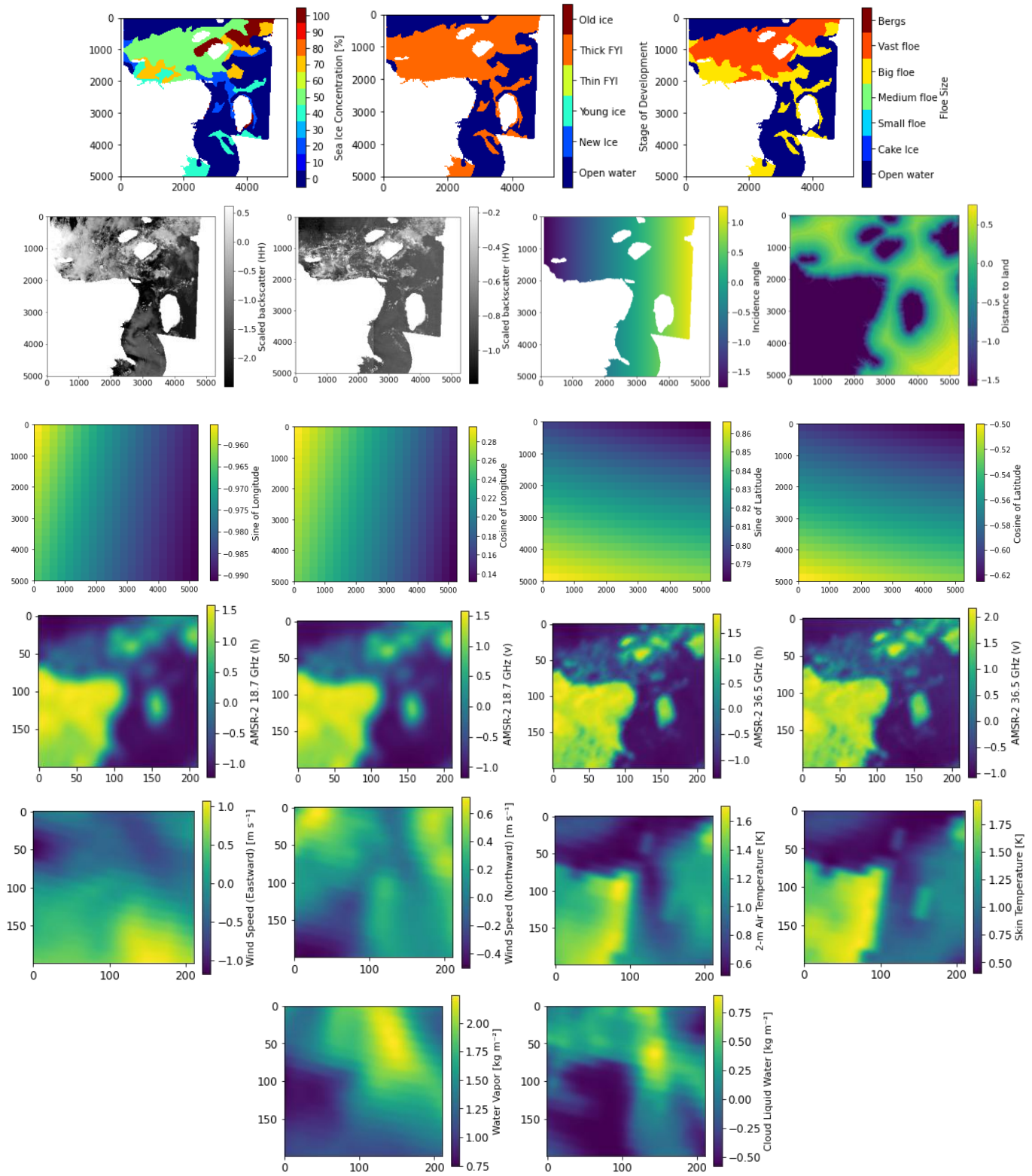


**Fig. 1.** Input channels and corresponding ice charts with auxiliary data for scene ‘20200701T114012\_cis\_prep.nc’. All input channels displayed here are provided in the benchmark dataset, except the four channels of sine and cosine of latitude and longitude, which we derive using the geospatial coordinates of each scene.

In this study, SAR variables (HH, HV, incidence angle), AMSR2 measurements at 18.7 and 36.5 GHz (V and H polarizations),

**Table 1**  
Observation groups used as input to the models

Observation Group	Variable description	Number of channels
SAR	HH, HV, Incidence angle	3
Location	Sinusoidal embeddings of longitude and latitude, distance map	5
AMSR2	Dual-polarized AMSR2 brightness temperature data at 18.7 and 36.5 GHz	4
ERA5 Weather Reanalysis	East- and Northward 10-m wind speed, 2-m air temperature, total column water vapor, total column cloud liquid water, skin temperature	6

distance map, latitude and longitude coordinates, and all ERA5 environmental variables are selected as the primary inputs to our model. Other AMSR2 variables are not included since the combination of 18.7 and 36.5 GHz frequencies resulted in the best performance according to (X. Chen et al., 2024b). In each NetCDF file, the dimensions of SAR images, distance maps, and ice charts are aligned, maintaining consistent geospatial coverage. Other variables in these files, however, have varying spatial dimensions and are resized to align with the dimensions of the corresponding SAR data and ice charts using the 'nearest neighbor' interpolation method. After interpolation, patches of size (768, 768) are extracted in the training scenes.

### 3.2. Sinusoidal Geospatial Encoder

To incorporate geospatial location into the deep learning model (to study its impact on signal disambiguation), we create geospatial encodings from the latitude and longitude of grid points. Geospatial encoders in deep learning have a common structure  $\text{Enc}(x) = \text{NN}(\text{PE}(x))$ , whereas the non-parametric positional embedding (PE) function transforms locations into a higher dimensional vector space to incorporate different spatial information that is more learning-friendly for the neural network  $\text{NN}(\cdot)$  (Liu and Biljecki, 2022; Mai et al., 2022; Rußwurm et al., 2023). The purpose of the neural network  $\text{NN}(\cdot)$  is to provide a learnable component to map the input position embedding into the geospatial encoding for capturing the complex relationship between input locations and target labels (Mai et al., 2022).

Aodha et al. (Mac Aodha et al., 2019) developed  $\text{Enc}_{\text{wrap}}(x) = \text{NN}(\text{PE}_{\text{wrap}}(x))$  which uses sinusoidal functions as positional embedding (PE) to wrap the geographic coordinates. The purpose of using sinusoidal functions is to wrap geographic coordinates around the world (Mai et al., 2022). In Equation (1), latitude and longitude values (ranging from 48.87 to 87.30 and -162.13 to 21.73 in our dataset, respectively) are first converted from degrees to radians and then are fed into sine and cosine functions.

$$\text{PE}_{\text{wrap}}(x) = \left[ \sin\left(\pi \frac{\lambda}{180^\circ}\right), \cos\left(\pi \frac{\lambda}{180^\circ}\right), \sin\left(\pi \frac{\phi}{90^\circ}\right), \cos\left(\pi \frac{\phi}{90^\circ}\right) \right] \quad (1)$$

where  $x = (\lambda, \phi)$ , with  $\lambda$  representing longitude and  $\phi$  representing latitude.

We incorporate a sinusoidal encoder as additional input channels and feed to the DeepLabV3 model, which increases the number of channels for longitude latitude coordinates from 2 channels  $[\lambda, \phi]$  to 4 channels  $[\sin\left(\pi \frac{\lambda}{180^\circ}\right), \cos\left(\pi \frac{\lambda}{180^\circ}\right), \sin\left(\pi \frac{\phi}{90^\circ}\right), \cos\left(\pi \frac{\phi}{90^\circ}\right)]$ . By transforming the coordinates (measured in radians) using the sine and cosine functions, cyclic representations that accurately reflect the periodic nature of geographic coordinates in the Arctic are reproduced. Therefore, for training the model, in total, we use a combination of 18 channels as illustrated in Table 1. A sample of SAR polarizations with auxiliary data from these channels for scene '20200701T114012\_cis\_prep.nc' are illustrated in Fig. 1.

## 4. Methods

First, we present the architecture of the model and training process to clearly contextualize our methodology in a reproducible way. Next, we explain the training and validation split and evaluating strategy. Then, we describe the ensemble techniques for improving performance. Lastly, we describe our implementation of Grad-CAM and Gradient SHAP for interpreting the models and to examine the contribution of each feature and pixel in the input for mapping various values of SIC, SoD, and FLOE.

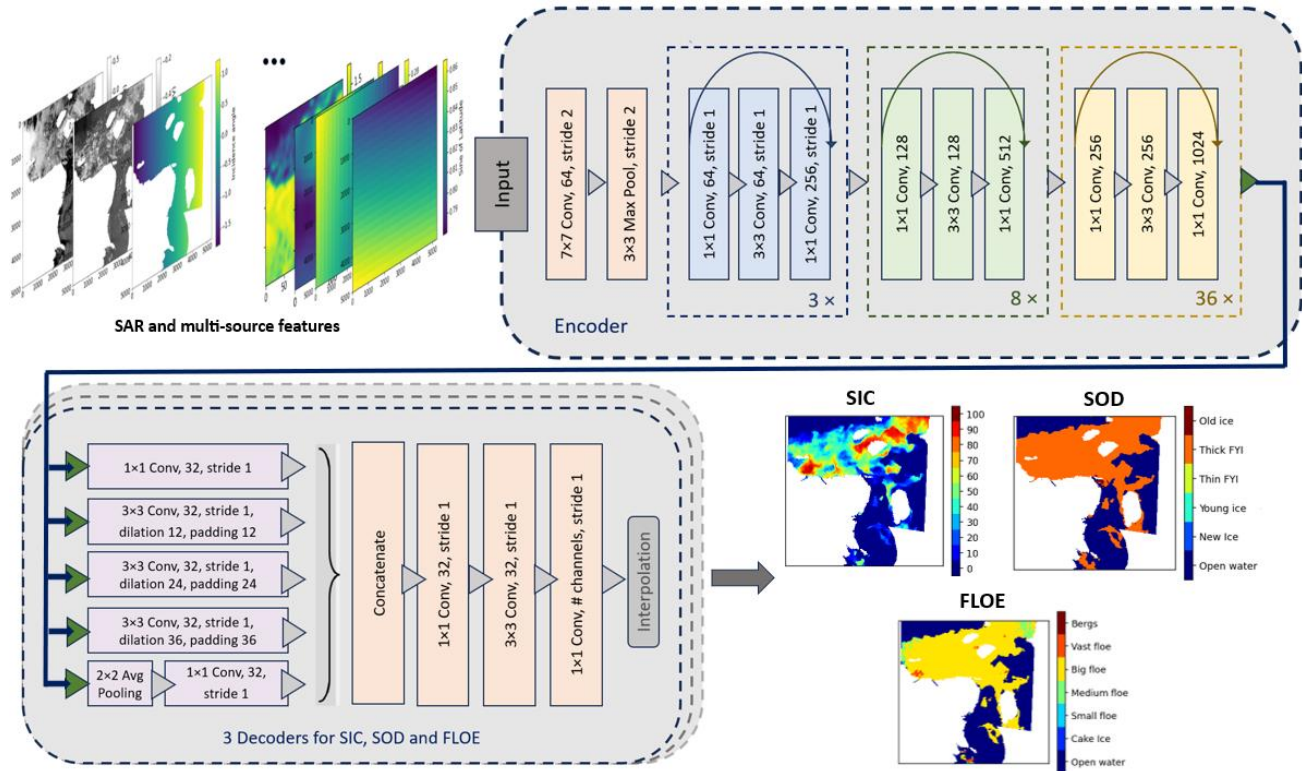


**Fig. 2.** Model architecture. A truncated ResNet-152 is used as backbone, followed by customized ASPP module with average pooling (instead of the default global pooling) to allow for training on sub-images and inference on full-scenes. One ASPP decoder module is used per each target of SIC, SoD, and Floe.

#### 4.1. Model Architecture

The architecture we use is an extension of (Pires De Lima and Karimzadeh, 2023). In our extended implementation, the model has an encoder and three separate parallel decoders to estimate SIC, SoD, and FLOE simultaneously as shown in Fig. 2. The encoder component of the model employs the first three blocks from ResNet-152 (three primary stages—layer1, layer2, and layer3). We discard the ResNet’s classifier and last convolutional block, because it results in better performance in our exploratory runs compared to using the full ResNet-152. We modify the first convolutional layer of the ResNet-152 to handle input with an expanded channel dimension of 18. The subsequent three decoders, customized for SIC, SoD, and FLOE are built on atrous spatial pyramid pooling (ASPP) (Chen et al., 2017), which incorporates dilated convolutions at three dilation rates [12, 24, 36] in addition to a 1x1 convolution layer to effectively capture multi-scale contextual information by leveraging both global and regional spatial contexts to further enhance performance. The atrous convolutions expand the receptive field of the filter without increasing the number of trainable parameters or downsampling the input features.

Additionally, we modify the ASPP module from PyTorch’s implementation to support images with varying dimensions during training and prediction by substituting the default global average pooling with average pooling, using a kernel size of  $2 \times 2$  and a stride of 2. The entire model has 46.12 M parameters, with the encoder (ResNet-152) initialized using pretrained ImageNet weights (version 1), and the decoders using random weights. During training, the input image is effectively downsampled by a factor of 16 by the encoder, while the decoder maintains the same spatial dimensions for the encoded feature maps. Following the ASPP module, four convolutional layers, each accompanied by batch normalization and the ReLU activation function are sequentially applied. The final convolutional layer in each decoder generates predictions for the corresponding sea ice parameter, with output channel depth tailored to the specific task: 1 channel for SIC regression task values, 7 channels (6 classes + 1 mask) for SoD classification, and 8 channels (7 classes + 1 mask) for FLOE classification. Then, the model applies bilinear interpolation to upsample the output from each decoder to align with the input spatial coverage.

#### 4.2. Training, Validation and Testing Methodology

The training process begins by randomly selecting 24 validation scenes from the AI4Arctic Challenge training scenes, ensuring that they replicate real-world scenarios with various class distributions across SIC, SoD, and FLOE charts. We train the model using 487

scenes training set, evaluate the model performance with 24 validation scenes during training, and then test the trained model on the 20 scenes specified by the AutoICE challenge as the held-out test scenes. To address memory restrictions and increase training sample variability, we train the model using a patch-based approach from the 487 scenes instead of using full scenes for training. Random selection of input patches of size 768×768 pixels is utilized which can be interpreted as a data augmentation approach commonly referred to as random-crop augmentation. During training, one scene and one patch within each of the 487 scenes in the dataset are randomly selected to be fed into the model. The random selection of scenes and patches continues until the required number is reached (487 scenes in our training dataset and 20 patches selected per scene). In each epoch, approximately 608 iterations of patches are selected randomly for training. There are a total of 9,740 patches in the entire training dataset. Each patch corresponds to a specific sample used in training the model. Training patches containing fewer than 30% masked pixels are retained, otherwise discarded. As mentioned earlier, invalid or masked pixels are set to 255. Loss functions and metrics ignore the masked pixels to ensure that the model is not using these pixels to train on. We train the models using a dual-NVIDIA RTX A5000 graphics processing unit (GPU).

We train the models using Mean Squared Error (MSE) as loss function for SIC (regression task) and Cross-Entropy as loss for classification tasks of SoD and FLOE. We use the Adam optimizer with a batch size of 16. The learning rate is initially set to 1e-5 and is reduced by a factor of 2 if the validation loss does not improve over 4 consecutive epochs, with a minimum threshold of 1e-8. After 80 epochs, if the validation loss shows no improvement, early stopping will terminate the training of the model. The model weights with the highest combined validation score are saved, and then utilized to create predictions for validation and test sets. We use the entire scene without patch mosaicking to calculate the loss values and performance metrics for the validation and test scenes. According to the AutoICE challenge, the model's performance is quantitatively evaluated using the R<sup>2</sup> metric for SIC and F1 scores for SoD and FLOE. The scores for the three sea ice parameters are combined into a single final score based on the weighting scheme (Stokholm et al., 2024) outlined in Table 2 and Equation 2.

$$\text{Combined Score} = \frac{2}{5} \times \text{Score}_{SIC} + \frac{2}{5} \times \text{Score}_{SoD} + \frac{1}{5} \times \text{Score}_{FLOE} \quad (2)$$

We use PyTorch, PyTorch Lightning, and Scikit-Learn as the primary libraries for developing our models and conducting the analysis. It is worth mentioning that we experimented with different encoder-backbones including DenseNet-169, EfficientNet-B3 to B7, ResNet (18, 50, 101), and ResNet integrated with a convolutional block attention module (CBAM), different optimizers such as Adam and stochastic gradient descent (SGD), different numbers of validation scenes and augmentation techniques, various batch and patch sizes, different learning rates and learning rate schedulers including cosine annealing and ReduceLROnPlateau, and we found the best results using the model architecture and pipeline described in the previous paragraphs. Then, we trained this model five times using different validation sets to verify the models' performance metrics against the stochastic nature of training deep learning models, as well as to create multiple models for the ensemble.

### 4.3. Ensemble Methods

Ensemble techniques combine predictions from multiple models to reduce model variance and enhance generalizability resulting in more accurate and reliable final predictions. Given that the state-of-the-art scores on the AutoICE challenge were generated using an ensemble of tens of models (X. Chen et al., 2024b; Stokholm et al., 2024), to have comparative results, we experiment with three different strategies to ensemble five models and generate final outputs. First, in a simple averaging approach, we combine the outputs of multiple pre-trained models for SIC, SoD, and FLOE by computing the mean of the probability outputs. Second, in a weighted averaging approach, the predictions for SIC, SoD and FLOE are weighted based on the normalized validation scores, which reflect the validation performance of each model. To normalize the weights for the classification tasks including SoD and FLOE, each model's validation score for a specific task is divided by the sum of all validation scores for that specific classification task (Equation 3). To assign weights for the regression task (SIC), we take the inverse of each model's scores (1 - validation score) to give higher influence on models with lower validation errors (Equation 4).

**Table 2**  
Evaluation metrics and respective weights in the final score

Sea ice parameter	Metric (%)	Weight in combined score
SIC	R <sup>2</sup>	2/5
SoD	F1	2/5
FLOE	F1	1/5

For the classification tasks  $t_1$  and  $t_2$ , the weight assigned to the  $i$ -th model is calculated as:

$$W_{i,t} = \frac{s_{i,t}}{\sum_{j=1}^n s_{j,t}} \quad (3)$$

For the regression task  $t_3$ , the weight assigned to the  $i$ -th model is calculated as:

$$W_{i,t} = \frac{\frac{1}{1-s_{i,t_3}}}{\sum_{j=1}^n \frac{1}{1-s_{j,t_3}}} \quad (4)$$

where  $w_{i,t}$  is the weight assigned to the  $i$ -th model for task  $t$ ,  $s_{i,t}$  represents the validation score of the  $i$ -th model for task  $t$ , which quantifies the model's performance on a held-out validation dataset using the  $R^2$  metric for SIC and F1 scores for SoD and FLOE, and  $n$  is the number of models.

Third, in another weighted averaging approach (Equation 5), the weights are derived by first taking the negative logarithm of the validation scores for each task, converting them into log scores, and then applying the softmax function to these log scores. Logarithmic scaling helps further distinguish between models with high and low performance by exaggerating the difference between the validation scores. This strategy ensures that models with higher validation performance (lower log scores) contribute more significantly to the final predictions. The weight  $w_i$  for the  $i$ -th model is calculated as:

$$W_i = \frac{e^{-\log(s_{i,t})}}{\sum_{j=1}^n e^{-\log(s_{j,t})}} \quad (5)$$

#### 4.4. Gradient-Weighted Class Activation Mapping (Grad-CAM)

Grad-CAM determines the contribution of each pixel in the input image for predicting a particular class. It utilizes the gradient information that flows into the final convolutional layer to generate the class discriminative localization map for this purpose (Selvaraju et al., 2017). To calculate  $L_{Grad-CAM}^c$ , first the gradient of the segmentation output for the target class  $c$ ,  $Y^c$  (prior to applying the softmax function), with respect to the  $k$ -th feature map  $A_{ij}^k$  at spatial location  $(i, j)$  of the final convolutional layer is computed. Subsequently, these gradients are subjected to global average pooling to derive the importance weight of each feature map,  $W_k^c$ :

$$W_k^c = f(x) = \frac{1}{Z} \sum_i \sum_j \frac{\partial Y^c}{\partial A_{ij}^k} \quad (6)$$

where  $Z$  represents the total number of pixels in the feature map. The weight  $W_k^c$  quantifies the importance of feature map  $A_{ij}^k$  in predicting the target class  $c$  by partially linearizing the deep network beyond the final convolutional layer. A weighted combination of the feature maps is then computed, followed by applying the ReLU function, to highlight the features that positively influence the prediction for the target class:

$$L_{Grad-CAM}^c = ReLU(\sum_k W_k^c A_{ij}^k) \quad (7)$$

The output is a coarse heatmap with spatial dimensions corresponding to the final convolutional feature map. To produce fine-grained, pixel-level saliency maps,  $L_{Grad-CAM}^c$  is upsampled to align with the dimensions of the input image. (X. Guo et al., 2022; Haciefendioğlu et al., 2022; Selvaraju et al., 2017).

#### 4.5. Gradient SHAP (Gradient Shapley Additive Explanation)

We evaluate our trained DeepLabV3 model (with geospatial encoding) through Gradient SHAP (Lundberg et al., 2017), a model-agnostic explainability technique. It calculates the contributions of each input feature to the predictions in each task and identifies the most important input features and their impact on the model's predictions for sea ice parameters. Gradient SHAP calculates SHAP values by suppressing noise through the use of SmoothGrad (Smilkov et al., 2017) while employing Integrated Gradient (IG) as a base (Kawauchi and Fuse, 2022). SmoothGrad generates samples with Gaussian noise applied to the input image of the model to smooth the input image. In Integrated Gradient, noise arises due to the linearity of the path integral. Integrated Gradients estimates feature attributions by computing the integral of gradients along the path from a given baseline to the actual input (Sundararajan et al., 2017):

$$IG_i(x) = (x_i - x'_i) \times \int_0^1 \frac{\partial F(x' + \alpha(x - x'))}{\partial x_i} d\alpha \quad (8)$$

where  $x'$  is the baseline input (such as a zero vector, a mean over training samples, or a black image),  $x$  is the actual input,  $\alpha$  is a scaling factor and  $\frac{\partial F}{\partial x_i}$  is the gradient of the model output  $F(x)$  with respect to the input feature  $x_i$ .

Gradient SHAP, on the other hand, maintains the nonlinearity of the path as it selects random points along the path and averages their outputs, and then further suppresses the noise using SmoothGrad (Kawauchi and Fuse, 2022). Gradient SHAP approximates SHAP values by averaging gradients over randomly sampled baselines. It perturbs each input sample with Gaussian noise multiple times, selects a random baseline from the baseline distribution, picks a random point along the interpolation path between the baseline and the input, and then calculates the gradient of outputs with respect to those selected random points. The final Gradient SHAP values are the expected value of gradients multiplied by the difference between inputs and baselines, where input features with positive Gradient SHAP values contribute positively to the model's output, and those with negative values contribute negatively. The magnitude reflects how strong the impact is.

In our study, we calculate Gradient SHAP attribution scores for the features in Table 1 including SAR HH, HV, incidence angle, sine of longitude, cosine of longitude, sine of latitude, cosine of latitude, distance map, AMSR2 measurements at 18.7 and 36.5 GHz (V and H polarizations), 10-m wind speed (eastward and northward), 2-m air temperature, skin temperature, total column water vapor, and total column cloud liquid water. These attributions are aggregated and normalized to ensure comparability among all the input features. We use the Gradient SHAP implementation from the Captum library's interpretability methods (Lundberg et al., 2017).

## 5. Experimental results and analysis

### 5.1. Ensemble Model Performance

This section describes the performance of ensemble methods using five model members that each was trained on different validation sets. For training the five members for each ensemble, we used a combination of 18 channels (all the input channels) listed in Table 1. The performance metrics obtained from the five member models and ensemble methods on the test set are summarized in Table 3. Each member was trained using a different training and validation split, but the Table shows the scores on the test set. The highest combined score (87.3%) is obtained using raw score weighted average, with relatively low error in

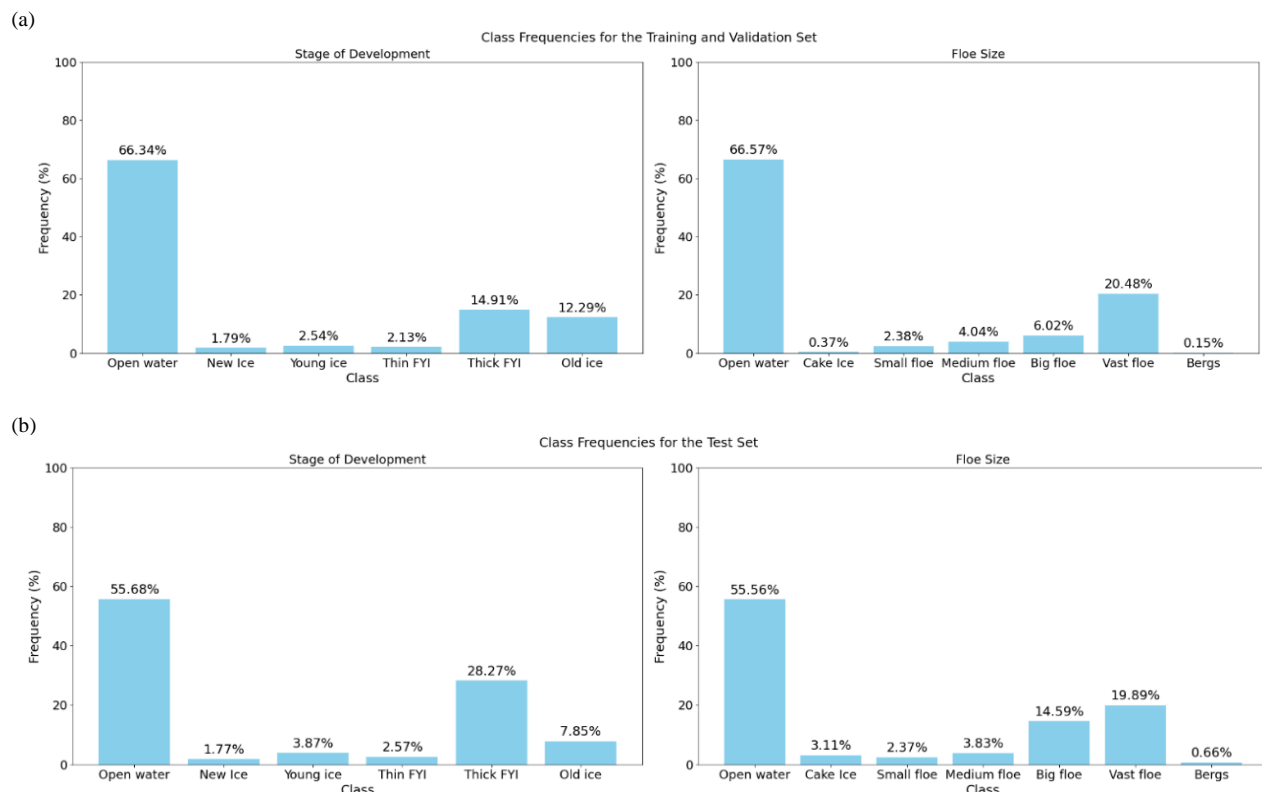


**Fig. 3.** Class frequencies for (a) the training-validation set and (b) the test set.

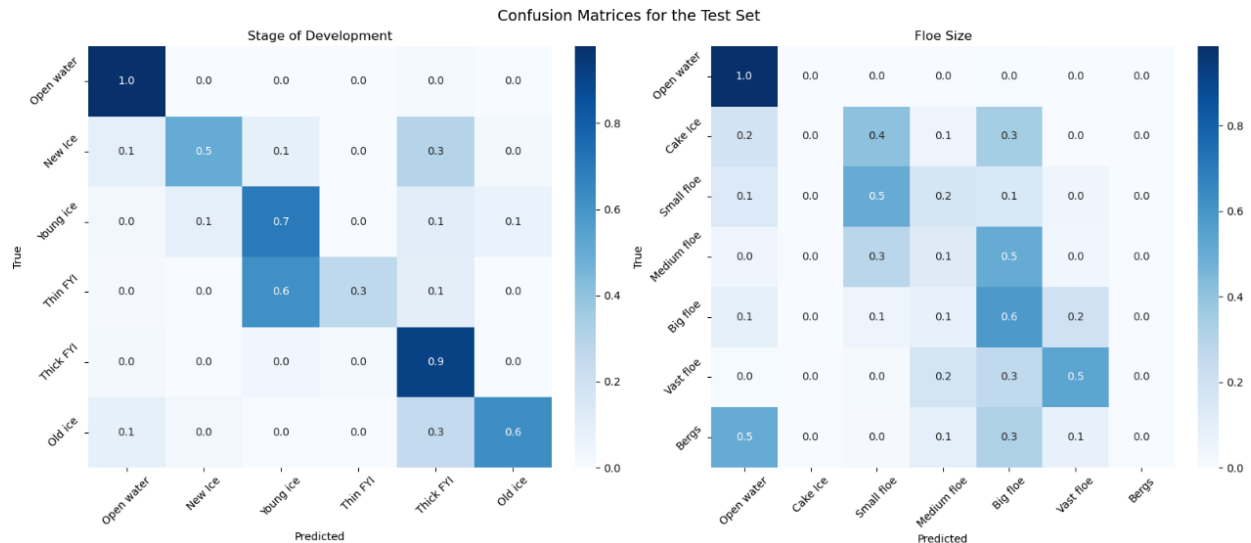


**Fig. 4.** Confusion matrices for SoD and FLOE on the test scenes for the ensemble model with raw weighting score averaging scheme.

**Table 3**  
Performance score of five member models and ensemble methods on the test set

Models	Test scores			
	Combined Score	SIC	SoD	FLOE
Validation set (1)	86.90%	90.31%	89.79%	74.30%
Validation set (2)	86.51%	90.35%	88.26%	75.32%
Validation set (3)	86.08%	89.75%	88.04%	74.81%
Validation set (4)	86.85%	91.16%	88.89%	74.15%
Validation set (5)	86.10%	90.92%	87.26%	74.13%
simple averaging	87.27%	91.33%	89.30%	75.11%
weighted averaging using raw scores	<b>87.3%</b>	<b>91.33%</b>	<b>89.35%</b>	<b>75.11%</b>
weighted averaging using log scores	87.26%	91.33%	89.27%	75.12%

estimating SIC ( $R^2$ : 91.33%) and strong performance in SoD (F1 score: 89.35%), surpassing the highest SoD score reported in published papers and the AutoICE challenge (88.61%), with the FLOE task yielding an F1 score of 75.11%. In Fig. 3. (a) and (b) the class frequencies for the Training-validation scenes (all the scenes except for 20 test scenes) and 20 test scenes are shown, respectively. The class distribution between the training/validation set and testing scenes for SoD and FLOE shows a significant imbalance, with open water predominating the dataset, particularly in the training/validation set. Fig. 4. shows the confusion matrices for SoD and FLOE for the ensemble model with a raw weighting score averaging scheme. Overall, the confusion matrix hand in hand with per-class sample distributions reveals two primary reasons for misclassification: class imbalance and signal ambiguity. As it relates to class imbalance, the ensemble model has lower performance on new ice and thin FYI, which have the fewest data samples in training and test sets among all classes. Open water classification has high recall with 100% correct predictions (although some new ice and old ice are misclassified as open water), followed by high recall for thick FYI, with 90% correct predictions. Both these classes have the highest number of data samples in the training and test sets, but also, thick FYI is more easily distinguishable on SAR imagery.

The confusion matrix for FLOE further highlights the lower overall performance on this task, especially with cake ice, icebergs, and medium floe. The relatively lower performance for these categories can also partially be attributed to the relatively rare occurrences of these classes in the training set, specifically cake ice and bergs.

**Table 4**  
Validation and test scores of the models trained with and without geospatial encoding

Our custom DeepLabV3	Validation				Test			
	Combined Score	SIC	SoD	FLOE	Combined Score	SIC	SoD	FLOE
<b>With Geospatial Encoding</b>	92.56%	93.93%	94.55%	85.85%	<b>86.90%</b>	90.31%	89.79%	74.30%
<b>Without Geospatial Encoding</b>	92.02%	93.90%	92.60%	87.11%	<b>81.82%</b>	89.89%	78.19%	72.96%

Another challenge is ambiguities between different specific classes. For instance, in SoD, 30% of old ice pixels are misclassified as thick FYI, or 60% of thin FYI pixels as young ice. In FLOE, 30% and 50% of medium floe pixels are misclassified as small floe and big floe, respectively, which are neighboring classes with medium floe. In the next section, we study the impact of using geospatial encoding to potentially improve lower performance metrics as a result of class imbalance or observation ambiguity.

### 5.2. Geospatial Encoding Effect and Feature Importance Analysis

Our results indicate that including geospatial encoding as features during training improves the SoD, FLOE, and SIC scores by 11.6%, 1.34%, and 0.42%, respectively, in the testing set as listed in Table 4. For these analyses, we present the results for singular training runs using the validation set (1) rather than ensembling, given that the differences with and without geospatial encoding are substantially large and the comparisons are not affected by stochasticity. Another reason for not ensembling the models (with/without geospatial encoding) are that in the next sections, we run these trained models individually through interpretability methods including Gradient SHAP and Grad-CAM to analyze, interpret, and compare the two models. These interpretability methods can only be run on single models. Gradient SHAP requires direct access to a single model's gradients to approximate feature contributions. Grad-CAM visualizes important regions in an input image by analyzing gradients from the final convolutional layers of a single model. Nevertheless, as mentioned before, the differences in model performance metrics (as shown in Table 4) are large enough to ensure that ensembling (or lack thereof) would not change the overall findings.

There are two potential explanations for why geospatial encodings are helping improve performance. One possible theory is that geospatial encodings help with disambiguation of ambiguous signals, since the backscatter coefficients of certain sea ice types often overlap significantly (Dierking, 2010; Partington et al., 2010; Zakhvatkina et al., 2017). The radar response of sea ice types is heavily influenced by environmental, melting and freezing conditions that can lead to ambiguities in radar signals. Since the AI4Arctic Sea Ice Challenge Dataset covers the period between January 2018 to December 2021 including melting and freezing seasons, backscatter coefficients for different ice types are more likely to be overlapping. However, while geospatial encoding is a predictor of sea ice conditions, it does not inherently reflect differences between the melting and freezing conditions unless temporal information is specifically incorporated into the model. This is because seasonal variations in the Arctic may cause sea ice to change between melting and freezing conditions. In addition to ambiguities, geospatial encoding seems to help with class imbalance too. Another potential theory is that the model is memorizing locations rather than relying on observations first. This would indicate potential problems with model generalizability to other datasets, regions and times, and would indicate that the scores obtained without geospatial encodings are more reliable indicators of model performance in other regions. Our results presented in the next section show that this explanation is more likely for certain ice types.

It is worth mentioning that all SIC, SoD, and FLOE tasks share the same ResNet encoder, however, the effect of geospatial encoding differs for each target modeling. Since the spatial distribution of ice types is influenced by their geographic location, certain sea ice types are more prevalent in specific regions such as old ice, which is mostly found on the Canadian archipelago, north and east coast of Greenland. Therefore, model memorization of spatial distribution of certain sea ice types increased the F1 score for SoD overall. However, an investigation of per-class performance is necessary to identify for which ice types this memorization is helping disambiguate observation signals, and for which ice types there is likelihood of pure model memorization regardless of observation signals, which would indicate problems for model generalizability.

1) *SoD*: To further investigate the effect of geospatial encoding on SoD classification, the confusion matrices for each model (a) with geospatial encoding and (b) without geospatial encoding are shown in Fig. 5. Removing geospatial encoding reduces correct classification across all classes in SoD including new ice (-20%), young ice (-40%), thin FYI (-40%), thick FYI (-20%), and old ice (-30%). As demonstrated in the confusion matrix (Fig.5 (b)), the model without geospatial encoding misclassifies a large portion of young ice and new ice as thick FYI (50%) and young ice (40%), respectively. Since Thick FYI and Old ice have overlapping signal ambiguities, adding geospatial encoding, contributes significantly to improving the model's capability to distinguish between them and improving mapping accuracy of Thick FYI and Old ice by correcting the misclassification.

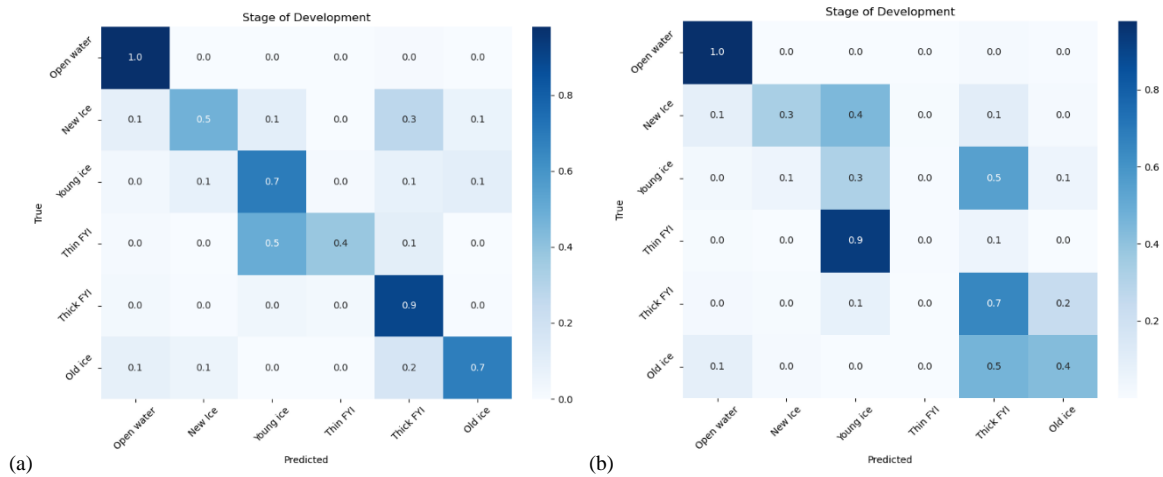


**Fig. 5.** Confusion matrices of SoD for each model (a) with and (b) without geospatial encoding.

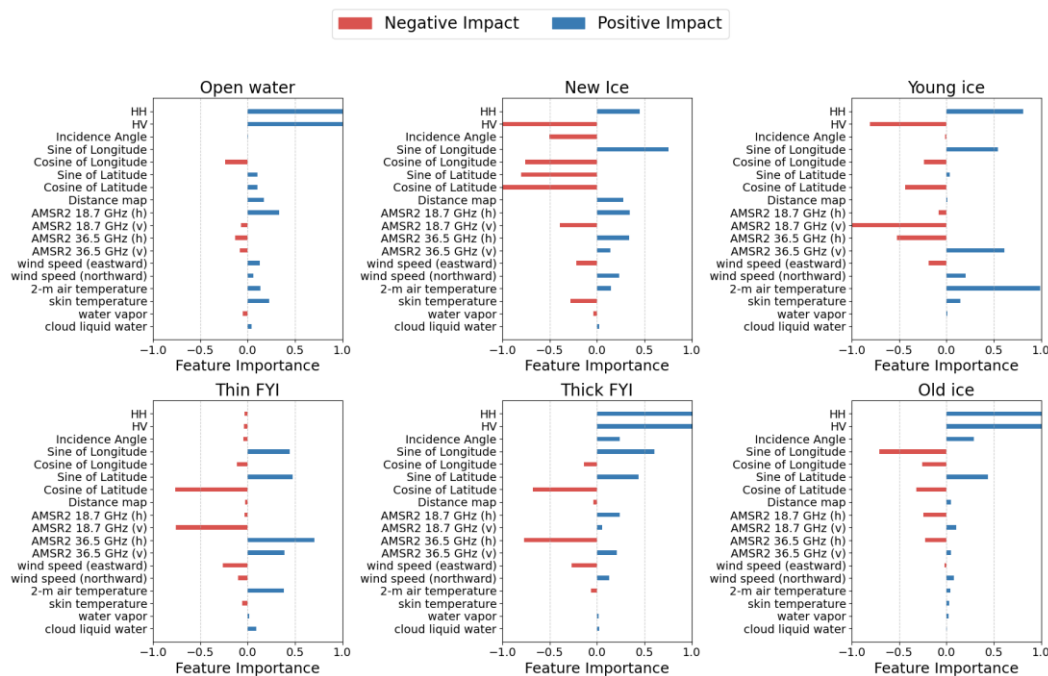


**Fig. 6.** Gradient-SHAP plot for SoD. Features with positive Gradient-SHAP values (blue colors) positively contribute to the model’s predictions for SoD, while those with negative values have a negative impact (red colors).

Gradient-SHAP analysis for SoD in Fig. 6. also shows geospatial encoding components (i.e., sine of latitude/longitude) have positive feature importance for most sea ice types. Notably, the importance of Sentinel-1 SAR HH and HV bands is very low in predicting thin FYI. For this specific class, the most important features are firstly those related to geospatial encoding, and then passive microwave AMSR-2. Put differently, the model seems to rely heavily on memorization of region based on geospatial encoding to classify thin FYI. The model without geospatial encoding completely misclassifies thin FYI pixels as young ice (90%) and thick FYI (10%). This indicates that while geospatial encoding is important in improving performance for thin FYI, the model is overly relying on them, and only then, some reliance on passive microwave observations. Therefore, it is likely that the model would not generalize to an entirely different region not covered by the AutoICE dataset, or the same region under different climate conditions in a specific year.

The lack of distinctive vertical features and sufficient training samples further amplifies the relatively higher importance of geospatial encoding for some classes. As expected, the HH channel has a positive contribution for classifying new and young ice which are typically flat, featureless horizontal surfaces, while the HV band is not identified as an important feature in Fig. 6. for these classes. Our findings are consistent with previous studies (Partington et al., 2010; Zakhvatkina et al., 2017), which indicated that HH polarization provides strong contrast between new ice and young ice due to its higher sensitivity to surface

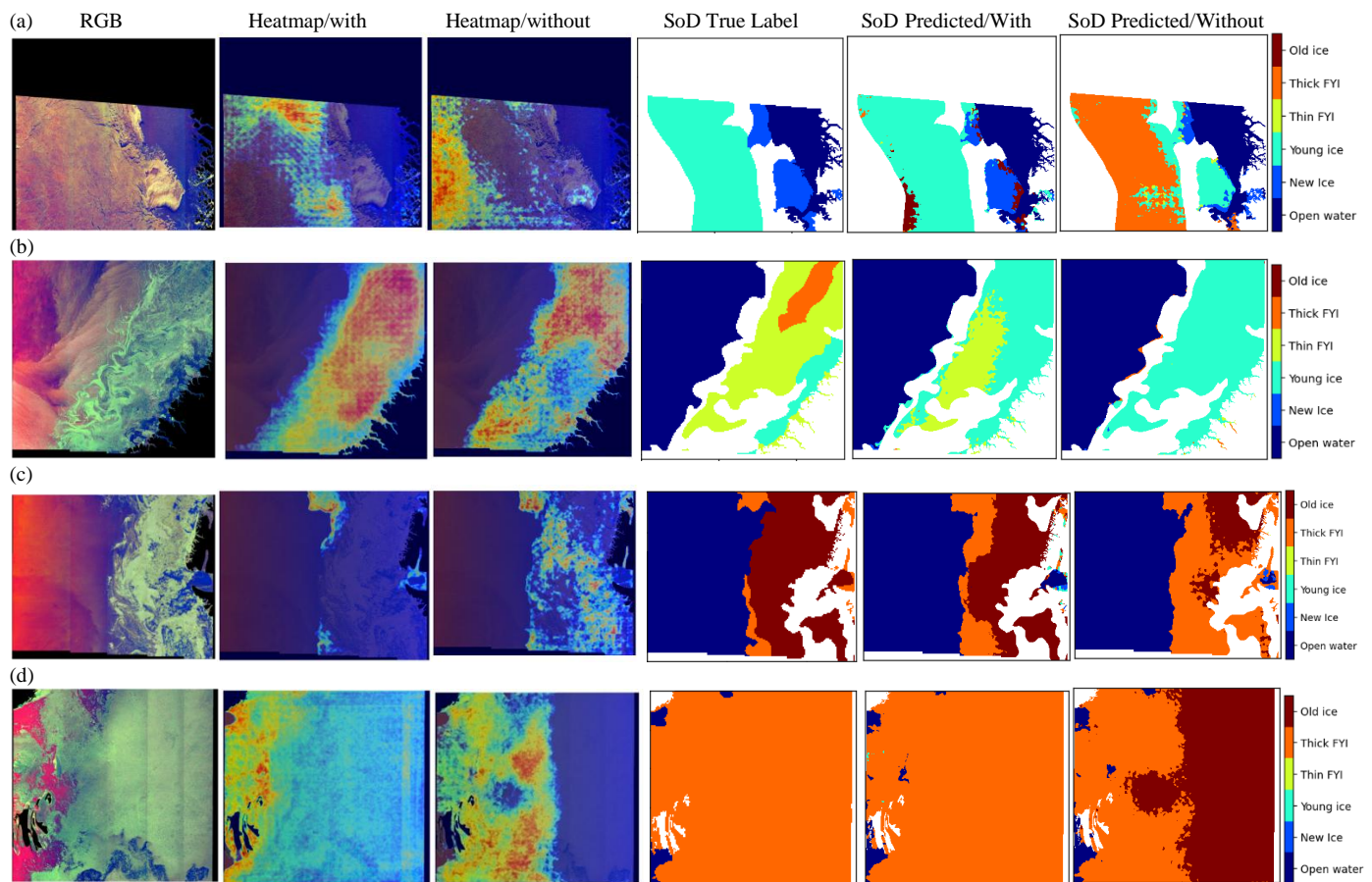


**Fig. 7.** False color images (RGB: HH, HV, and HH/HV) from the test set with the corresponding labels, predicted charts, and Grad-CAM heatmaps obtained from the models trained with and without geospatial encoding. Grad-CAM heatmaps are for different classes of interest: (a) Young Ice, 20211212T211242\_dmi\_prep, (b) Thin FYI, 20200217T102731\_cis\_prep, (c) Thick FYI, 20210506T075557\_dmi\_prep, (d) Thick FYI, 20180623T114935\_cis\_prep. Areas that are land or without labels due to low concentration according to the benchmark criteria are masked in white.

scattering differences (Song et al., 2021). In addition, Song et al. (Song et al., 2021) demonstrate that for identifying new ice (<10 cm) and young ice (10–30 cm) the classification accuracies with HH signals are significantly higher than HV signal. Their study also indicates minimal differences between HH and HV channels for classifying medium FYI (70–120 cm) and thick FYI (>120 cm) (Song et al., 2021) which agree with our findings for identifying thick FYI and old ice. This might indicate that geospatial encoding can help the misclassification problem of specific sea ice types resulting from the backscatter coefficients’ distribution overlap when surface roughness features are missing, or when roughness features are more similar, by relying on the spatial distribution of sea ice types. For instance, as illustrated in the confusion matrices (Fig. 5.), without geospatial encoding, 50% of old ice are misclassified as thick FYI, but geospatial encoding decreased the misclassification rate of old ice as thick FYI to 20%. For both these classes, both HH and HV bands have high feature importance, followed by geospatial encoding and AMSR-2 bands which help in disambiguation, albeit better disambiguation when geospatial encoding is present.

Fig. 7. illustrates Grad-CAM heatmaps obtained from the models with and without geospatial encoding for different test files and classes of interest including (a) new ice and young ice, (b) Thin FYI, (c) Thick FYI, (d) Thick FYI and Old ice, overlaid on the corresponding false color images (RGB: HH, HV, and HH/HV). To enhance interpretation and facilitate comparison, the corresponding labels and predicted ice charts from the models are included. Grad-CAM’s final output is a heatmap, highlighting the specific areas of an input image that contribute most to the model’s predictions for each target. It is worth noting that Grad-CAM analyzes the gradients of the last feature maps of the convolutional network and does not directly attribute to the specific input channel. Therefore, it provides a complementary view to the Gradient-SHAP presented in Fig. 6. Fig. 7. (a) shows that the heatmap obtained from the model with geospatial encoding has strong activation in regions where young ice is present, while the other heatmap shows strong activation in irrelevant regions for young ice. In Fig. 7. (b) the heatmaps highlight the areas that contain thin FYI class, but the heatmap obtained from the model without geospatial encoding is less focused on that area, and consequently, misclassifies thin FYI as young ice. However, looking at the Gradient-SHAP analysis in Fig 6, it is clear that the reason beyond those geographic areas paid more attention to (in the case of thin FYI in Fig. 7. (b)) is primarily due to the attention paid to geospatial encodings as important features (rather than SAR observations), which may result in lack of

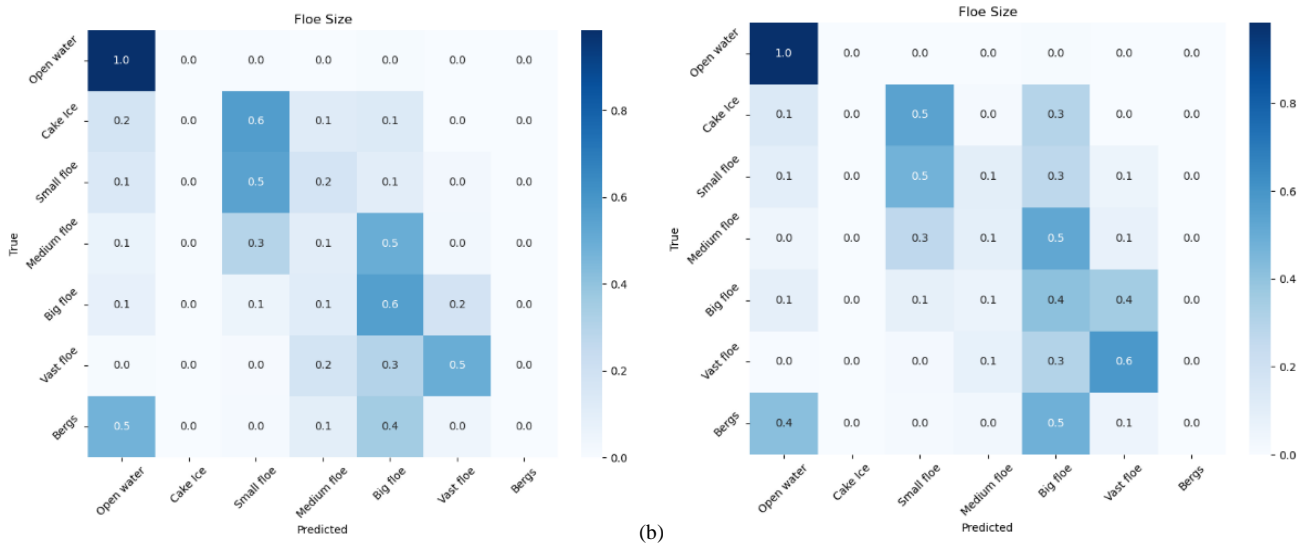


**Fig. 8.** The confusion matrices of FLOE for each model trained (a) with geospatial encoding and (b) without Geospatial encoding.

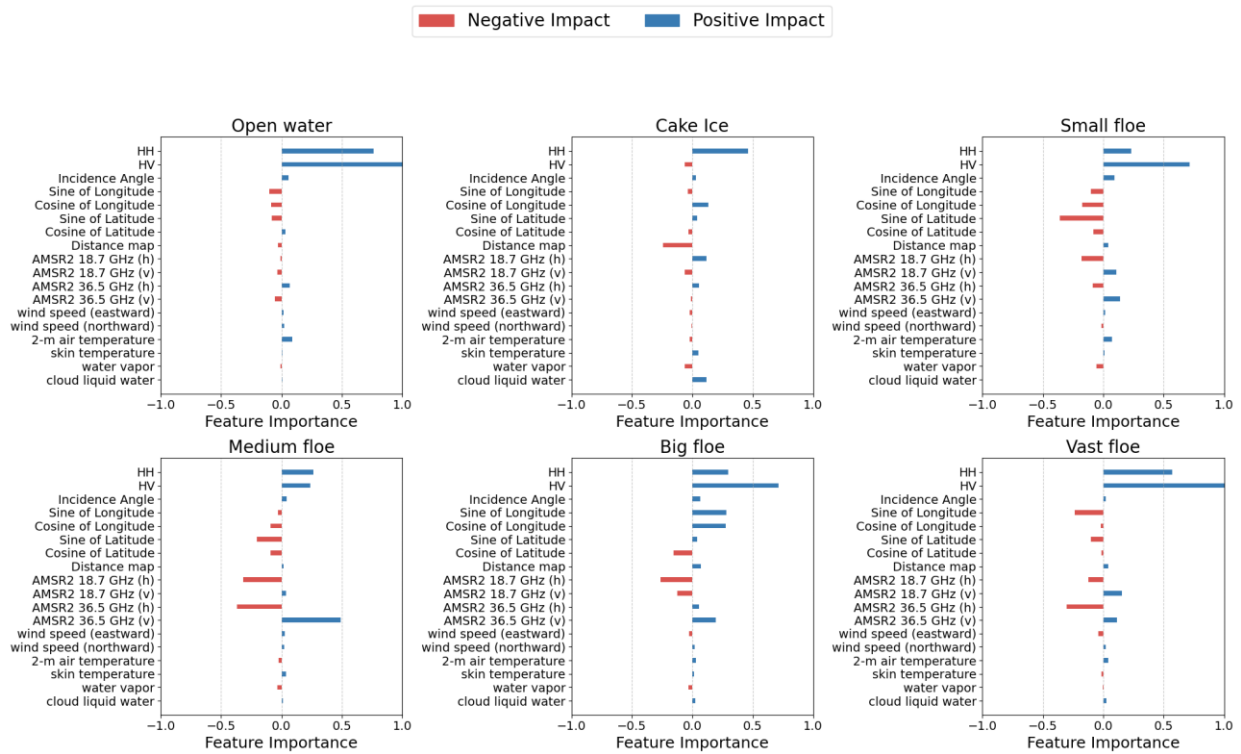


**Fig. 9.** Gradient-SHAP plot for FLOE. Features with positive Gradient-SHAP values (blue colors) positively contribute to the model’s predictions for FLOE, while those with negative values have a negative impact (red colors).

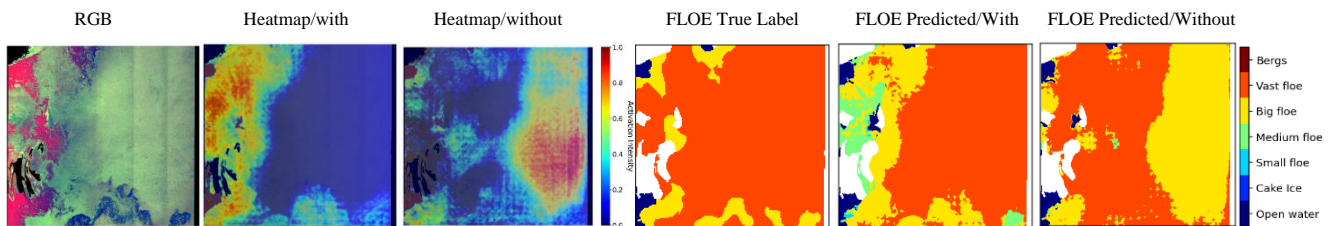


**Fig.10.** False color image (RGB: HH, HV, and HH/HV) from the test set with the corresponding label, predicted charts, and heatmaps obtained from the models trained with and without geospatial encoding for big floe class: 20180623T114935\_cis\_prep.

generalizability to other regions. Fig. 7. (c) and (d) heatmaps obtained from the model with geospatial encoding show that the model focuses on areas in the 20210506T075557\_dmi\_prep and 20180623T114935\_cis\_prep scenes that contain thick FYI and indicates training with geospatial encoding improves the model performance in differentiating between thick FYI and old ice. This indicates that geospatial features are helping the model to make its decision on thick FYI and distinguish between thick FYI and old ice. It is worth analyzing the contribution of other features in SoD. Gradient-SHAP plot (Fig. 6.) shows the relative importance of AMSR-2 variables at frequencies 18.7 and 36.5 GHz for classifying new ice, young ice, and thin FYI by providing complementary information to HH and HV SAR channels and mitigating ambiguities in backscatter values. This indicates the value of passive microwave data in the disambiguation of thinner sea ice types. As Nakata et al. (Nakata et al., 2019) point out passive microwave radiometers are highly effective tools for detecting thin ice thickness. For instance, Makynen et al. (Makynen and Simila, 2022) used AMSR-2 to detect thin sea ice (thickness < 0.2 m) in the Arctic Ocean and X. Chen et al. (X. Chen et al., 2024b) observed a reduction in their model performance to classify new ice ( $\leq 10$  cm) and young ice (10-30 cm) when they removed AMSR2 data. In addition, brightness temperature has the ability to contrast between newly formed, young and FY ice, as demonstrated by (Scott et al., 2014; Zabolotskikh and Azarov, 2022), who state that the 6.9 GHz to 36.5 GHz frequencies can detect sea ice thickness up to 50 cm. Among Environmental variables, the 2-m air temperature has a small but positive contribution for detecting open water, new ice, specifically young ice, and thin FYI, due to its disambiguation potential for identifying freezing and melting processes. In addition, wind speed also has a very small positive impact on model performance for all classes except thin FYI.

2) *FLOE*: To further investigate the effect of including geospatial encoding on FLOE classification, the confusion matrices obtained from (a) the model trained with geospatial encoding, (b) the model without them are illustrated in Fig. 8. The model with geospatial encoding shows an improvement in correct classification by 20% for big floe class. The Gradient SHAP plot in Fig. 9. also demonstrates that geospatial encodings help with mapping big floe more than they do for vast floe, which is more frequent in the training data. In the case of FLOE, (unlike SoD), we do not observe concerning signs of model memorization purely based on geospatial location, and rather, more attention is paid to observations rather than location, which points to the disambiguating nature of geospatial encoding for this task. Compared to SoD, the importance of HH and HV polarizations in FLOE are more dominant than other features in general, except for medium floe. In classifying most floe types, the HV polarization has a stronger contribution than HH, possibly due to its sensitivity to volume scattering and contrast between different floe sizes' signatures. Toyota et al. (Toyota et al., 2021) also illustrated that both HH and HV signals are influenced by floe size and deformed ice, although the HV signal is more sensitive to the effects of floe size. Gradient SHAP also shows a very small contribution of the HH channel for Cake Ice, which is significantly underrepresented in the dataset, even though the confusion matrix shows a recall of zero. This highlights that Gradient SHAP still computes how each input feature affects the Cake Ice logit, even if the final classification does not reach the argmax.

Among AMSR-2 bands, the 36.5 GHz frequency in vertical polarization has a positive contribution to classifying different floe sizes including small floe, medium floe, big floe, and vast floe by providing complementary information to HH and HV channels to distinguish the differences between these floe types. This feature importance analysis depicts that environmental variables are not important features and do not affect model's performance for classifying floe types. Fig. 10 demonstrates false-color image (RGB: HH, HV, and HH/HV) from the test dataset (20180623T114935\_cis\_prep scene) with the corresponding label, predicted charts and heatmaps based on the models trained with and without geospatial encoding. The misclassifications between big floe and vast floe are reduced when geospatial encoding is included, when the model is focusing more on the regions where big floe pixels are present, unlike the model without geospatial encoding which has strong activation values in areas where vast floe pixels are present.

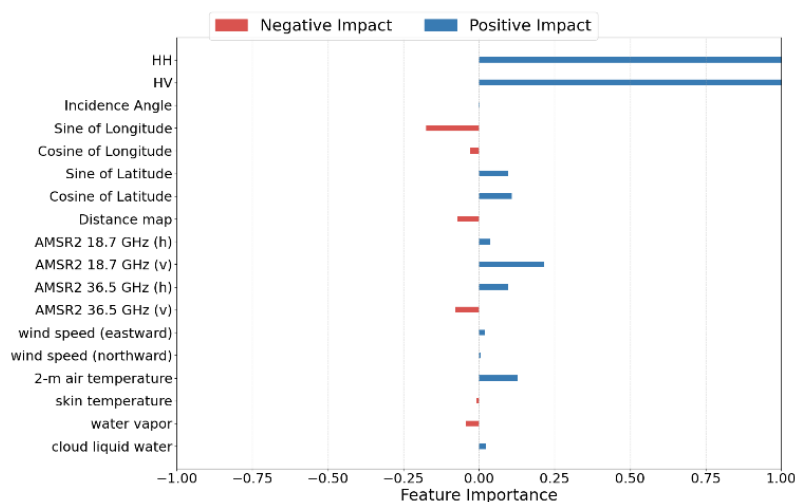


**Fig. 11.** Gradient-SHAP analysis for SIC. Features with positive Gradient-SHAP values (blue colors) positively contribute to the model’s predictions for SIC, while those with negative values have a negative impact (red colors).

3) *SIC*: Gradient-SHAP analysis for SIC (regression task) is shown in Fig. 11. HH and HV channels are the most important features. Between AMSR-2 variables, 18.7 (v) and 36.5 (h) GHz frequencies have positive contribution to the model’s SIC prediction. Among environmental variables, the 2-m air temperature is relatively important. Geospatial encoding has a positive but small contribution, and removing it reduces the  $R^2$  score for SIC by around only 0.42%.

### 5.3. Spatial Cross-Validation

In this section, we conduct two experiments to examine the effect of using geospatial encoding on the model generalizability when testing on distinct and non-overlapping regions relative to the training data. We use 512 scenes (the AI4Arctic training scenes) located in the Greenland (blue squares) and Canadian Arctic (red squares) as illustrated in Fig. 12. In the first experiment, we train our DeepLabV3 model with and without geospatial encoding on the Greenland Arctic scenes consisting 302

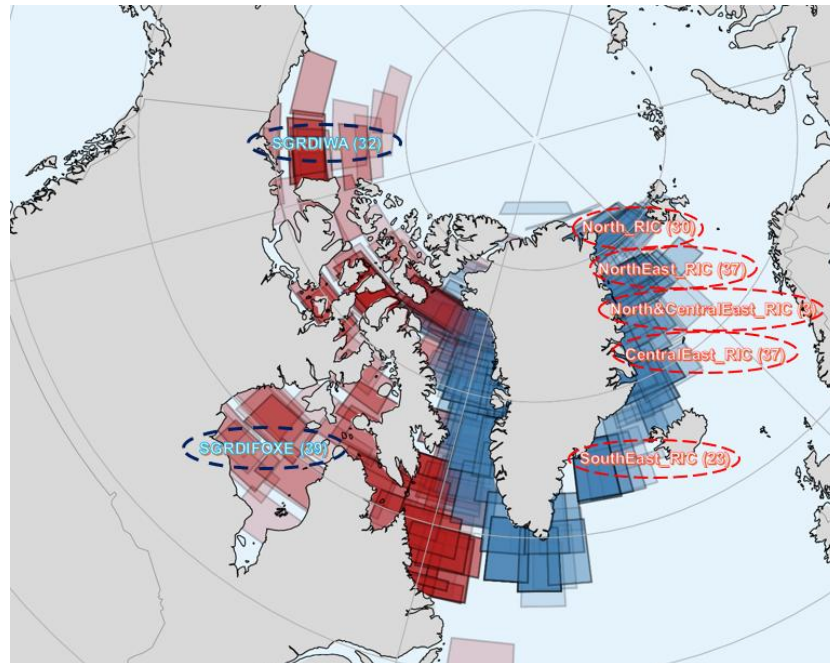


**Fig. 12.** An overview of all the scenes except for 20 test scenes in the AutoICE Challenge Dataset. Blue and red squares show scenes located in the Greenland and Canadian Arctic, respectively. Blue oval outlines indicate test on the Canadian subset and red oval outlines indicate test on the Greenland Arctic subset.

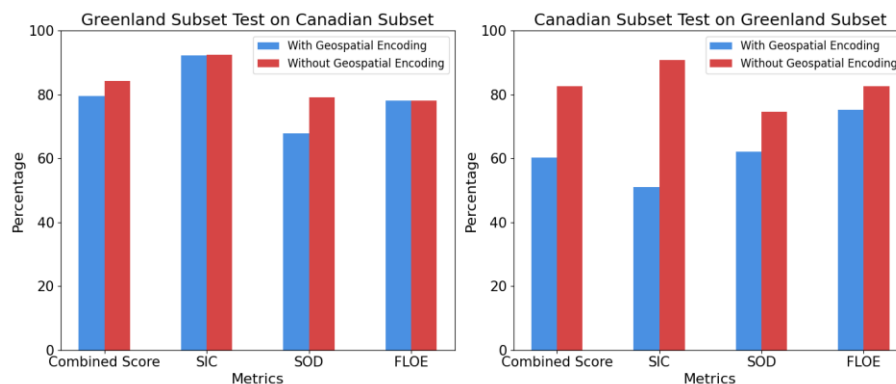


**Fig. 13.** Spatial cross-validation metrics for models trained with and without geospatial encoding. Training with geospatial encoding leads to considerable degradation in scores for deploying the model in unseen areas.

training and 13 validation scenes, and test on the Canadian subset (scenes specified as blue ovals in Fig 12). In the second experiment, we train the model with and without geospatial encoding on the Canadian Arctic consisting of 184 training and 13

validation scenes, and test on the Greenland Arctic subset (scenes specified as red ovals in Fig. 12.). The performance metrics obtained from these models on the test sets are illustrated in Fig. 13. Results show that the models trained with geospatial encoding, which showed improved performance on the benchmark test set have lower performance when testing on different and non-overlapping regions relative to the training data. This indicates that adding geospatial encoding hurts the model’s generalizability severely when deployed on an entirely different area or potentially the same area under different climate conditions due to model memorization and overfitting to the specific locations of sea ice parameters in the training regions.

In other words, the model starts learning and memorizing the specific geographic coordinates of sea ice parameters and relies on them to make predictions instead of or more than learning observation signals (i.e., HH, HV) that generalize across regions (see Section 5.2. Geospatial Encoding Effect and Feature Importance Analysis for more discussions on this). This indicates that the previously reported AutoICE results on the different benchmark test set as part of the competition may be potentially misleading, due to score inflation as a result of apparent improvement due to model memorization of regions. Therefore, we recommend spatial cross-validation as additional means for evaluation, and recommend against using geospatial encoding for this benchmark dataset, to ensure model performance and generalizability in other regions not covered by the dataset. Additionally, we recommend using interpretability methods to identify the most important features used in the models’ decision making, which allows for identifying potential issues with over-reliance on location features.

#### 5.4. Seasonal Performance Evaluation

We conduct an additional experiment to evaluate the model performance in different seasons. We select scenes into the freezing (January-March), and the melting (July-September) subsets. We train our DeepLabv3 model (without incorporating geospatial encoding) on 197 Canadian scenes (from all seasons) and test on freezing and melting scenes in Greenland, using 64 freezing and 68 melting scenes, to ensure that test scenes are not seen during training. Table 5 shows  $R^2$  scores for SIC and F1 scores for SoD and FLOE obtained across the melting and freezing seasons. The  $R^2$  score for SIC obtained from the test scenes in the freezing season is 8.754% higher than the test scenes in the melting season, since melt conditions are generally more challenging for sea ice mapping with SAR due to surface melt. However, on the freezing test scenes the F1 score for SoD is 70.96%, compared to 89.28% for melting scenes. It is worth mentioning that this is not just a result of model performance, but also the inevitable class variation in different subsets.

In Fig.14 (a) and (b) the class frequencies for the test scenes and the confusion matrices for SoD and FLOE in the melting season are shown, respectively. Furthermore, the distribution of backscattering coefficients for HH and HV polarization extracted from the SoD classes in the 68 melting scenes are presented in Fig 15. The class distribution between the test scenes for SoD and FLOE shows a significant imbalance, with open water predominating the dataset. For SoD, thick FYI and old ice have the highest number of samples in the test sets between the ice types. Open water classification has high recall with 95% correct predictions (although some new ice and thick FYI are misclassified as open water), followed by high recall for thick FYI and old ice with 70% and 65% correct predictions, respectively. As shown in Fig. 14 (b), in SoD, 33% of old ice pixels are misclassified as thick FYI or 42% of new ice pixels are misclassified as thick FYI, partly due to overlapping signatures of these ice types (in large sea ice chart label polygons, that include mixed ice types) as demonstrated in our results in Fig. 15. However, it is worth remembering that CNN models also use spatial context in addition to raw pixel values, and therefore, despite this large amount of overlap between signals, the model still achieves high scores. The results are consistent with the physics of sea ice. During the melt season, liquid water in the snowpack and on top of the ice layer decreases microwave signal penetration and ice type distinction (Tavri et al., 2023). The presence of liquid water changes dielectric permittivity, and due to variations in wind-wave-induced surface roughness from the water surface in melt ponds, HH and HV signatures from FYI and MYI frequently overlap (Barber et al., 2001; Tavri et al., 2023). The similar challenges affecting SoD classification in the melt season also impact FLOE classification. In FLOE, 28% of vast floe pixels, 68% of medium floe and 57% of small floe pixels are misclassified as big floe.

**Table 5**  
Evaluation of model performance across the melting and freezing seasons.

Test Scenes	Test scores			
	SIC	SoD	FLOE	Combined Score
<b>Melting season</b>	85.687%	89.28%	86.295%	87.246%
<b>Freezing season</b>	94.441%	70.96%	86.968%	83.554%

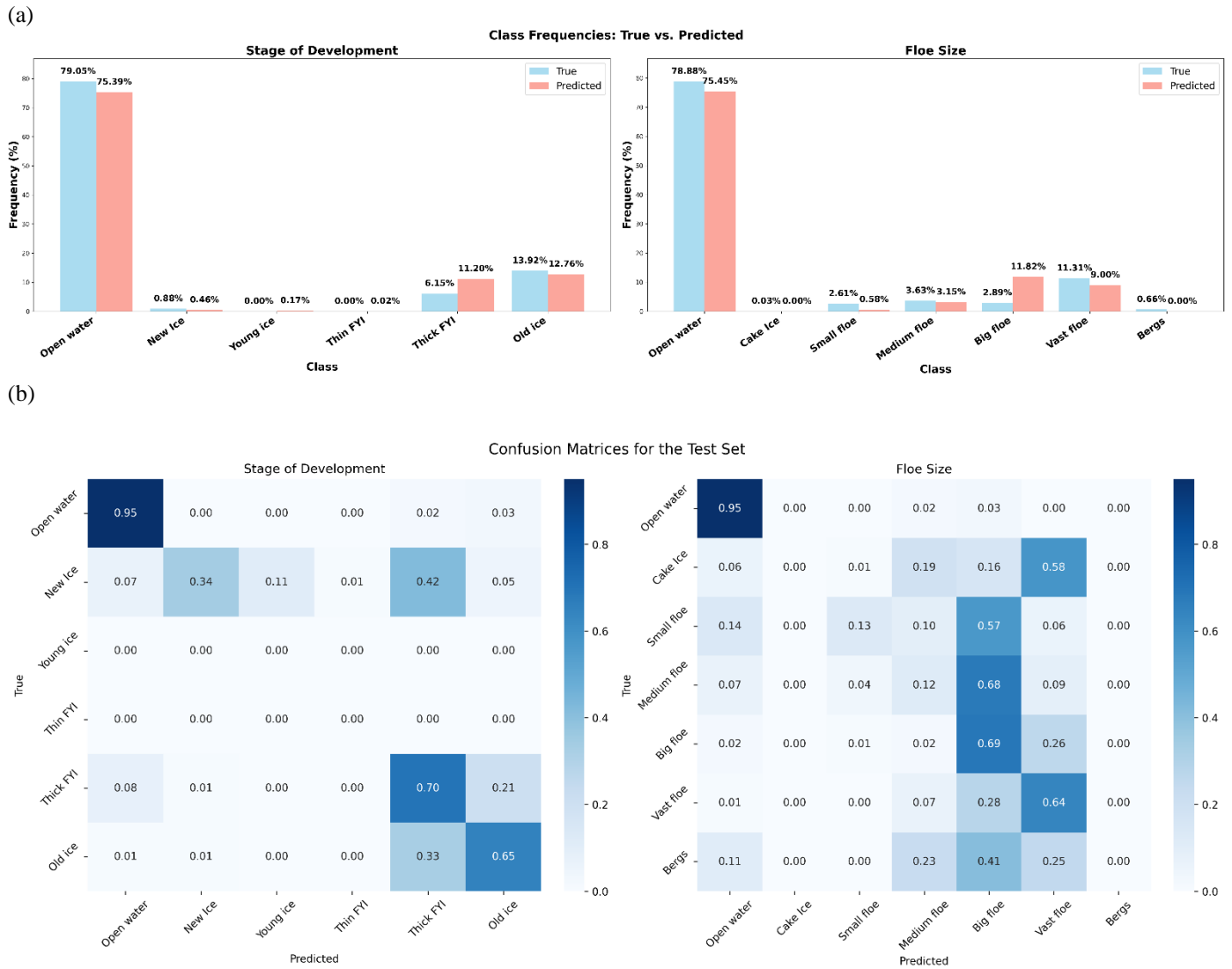


Fig. 14. (a) Class frequencies in the 64 melting test scenes and (b) the confusion matrices for SoD and FLOE in the melt test scenes.

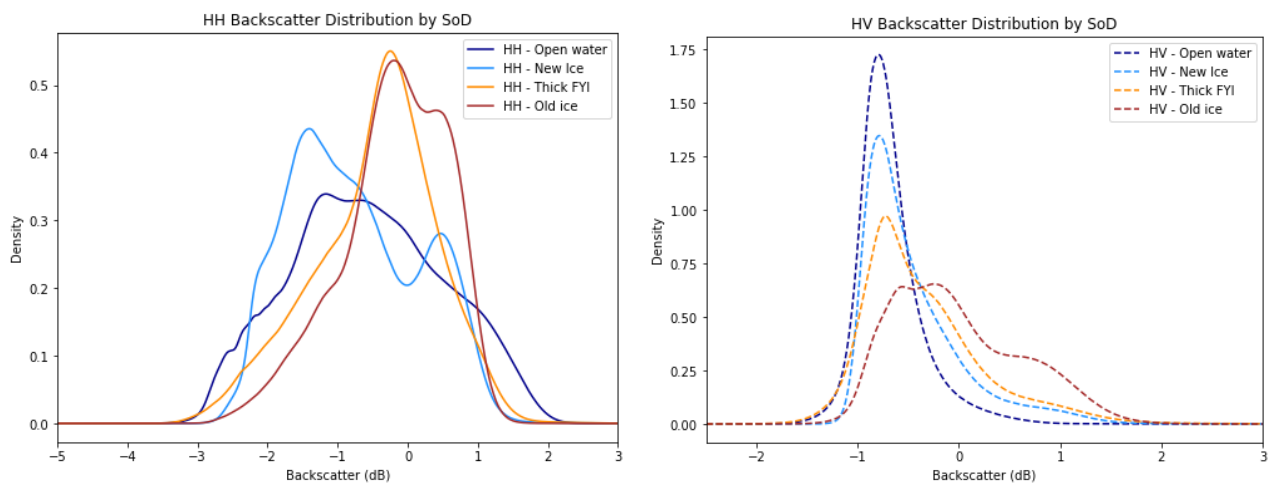


Fig.15. the HH and HV backscatter distribution of SoD classes in 68 melting scenes (in the ready-to-train version of the AutoICE Challenge dataset, the HH and HV backscatter values are standard-scaled using the mean and standard deviation of all training data within each polarization channel).

In Fig. 16 (a) and (b), the class frequencies for the test scenes and the confusion matrices for SoD and FLOE in the freezing season are shown, respectively. In addition, the distribution of backscattering coefficients for HH and HV polarization extracted from the SoD classes in 64 freezing scenes are presented in Fig. 17. In SoD, open water (51.94%), thick FYI (22.18%), old ice (19.85%) and thin FYI (4.89%) have the highest number of data samples in the test sets, respectively. As shown in Fig. 16 (b)., in SoD, open water classification has high recall with 97% correct predictions, followed by high recall for thick FYI with 82% correct predictions. However, the results demonstrate that 67% of old ice, 54% of thin FYI, 58% of young ice, and 46% of new ice pixels are misclassified as thick FYI, partially, again, due to overlapping signatures of different SoD classes as demonstrated in our results in Fig. 17. In freezing conditions, the backscattering characteristics of FYI in C-band SAR imagery are mainly affected by surface scattering and the presence of brine-rich frost flowers and/or saline snow. This can lead to a stronger backscatter coefficient for new/young ice and thin FYI, causing frequent overlap with the HH and HV signatures of thick FYI or old ice and the misclassification of these ice types (Isleifson et al., 2018; Onstott, 2011). In the freezing test scenes, in FLOE, open water (49.23%) and vast floe (43.61%) have the highest number of data samples in the test sets, respectively. For FLOE, open water classification has high recall with 98% correct predictions, followed by high recall for vast floe with 77% correct predictions. Also, similar patterns of misclassification, partially due to overlapping backscatter signatures are observed in FLOE confusion matrix, where small, medium, and big floes show significant confusion.

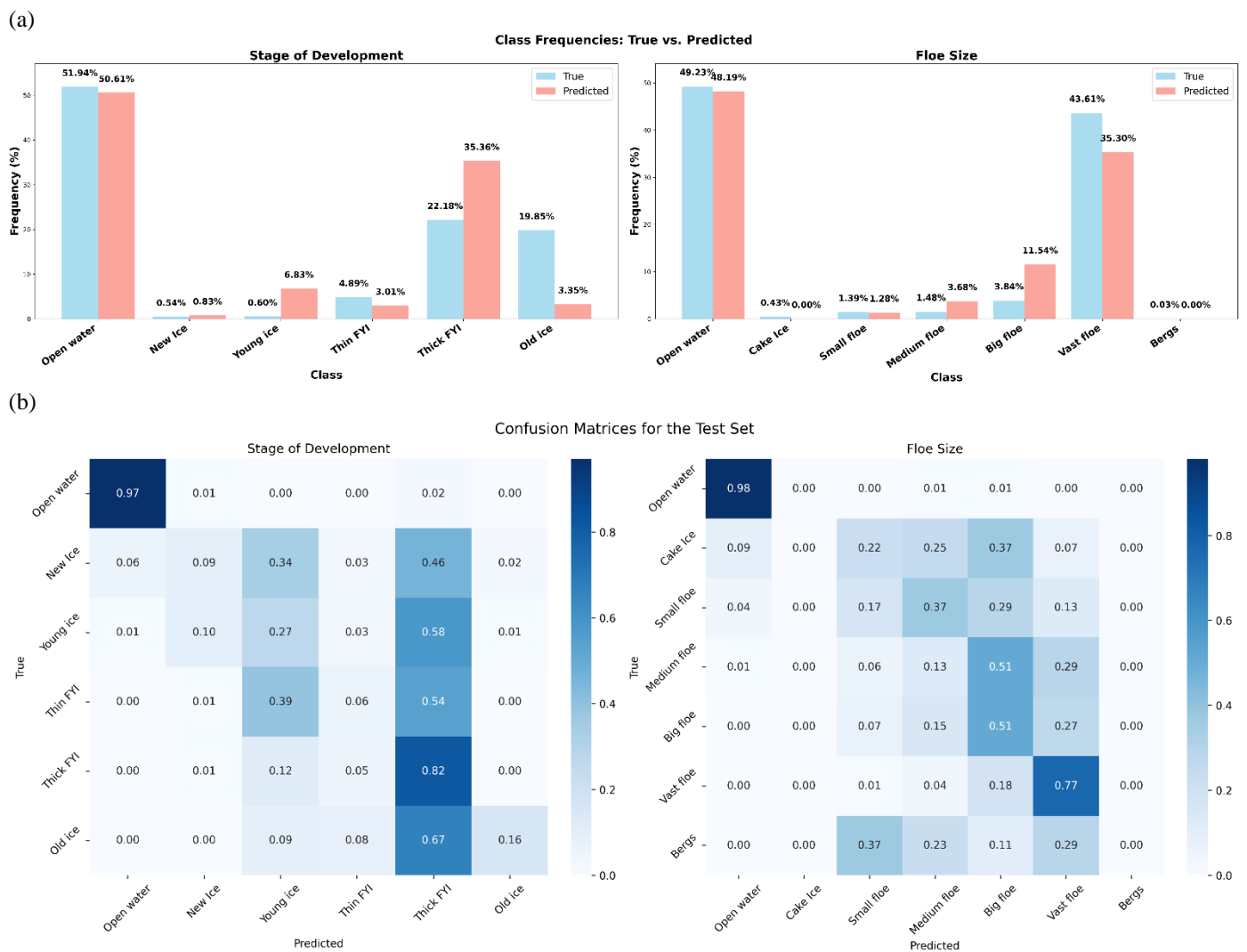


Fig. 16. (a) the class frequencies for the 64 freezing test scenes and (b) the confusion matrices for SoD and FLOE for these scenes.

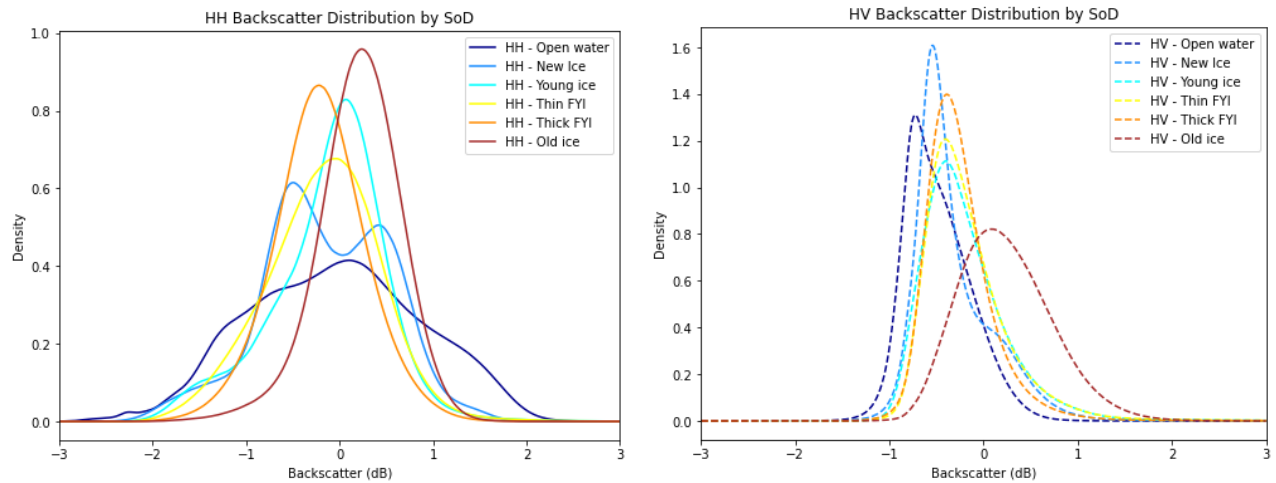


Fig. 17. the HH and HV backscatter distribution of SoD classes in 64 freezing scenes (in the ready-to-train version of the AutoICE Challenge dataset, the HH and HV backscatter values are standard-scaled using the mean and standard deviation of all training data within each polarization channel).

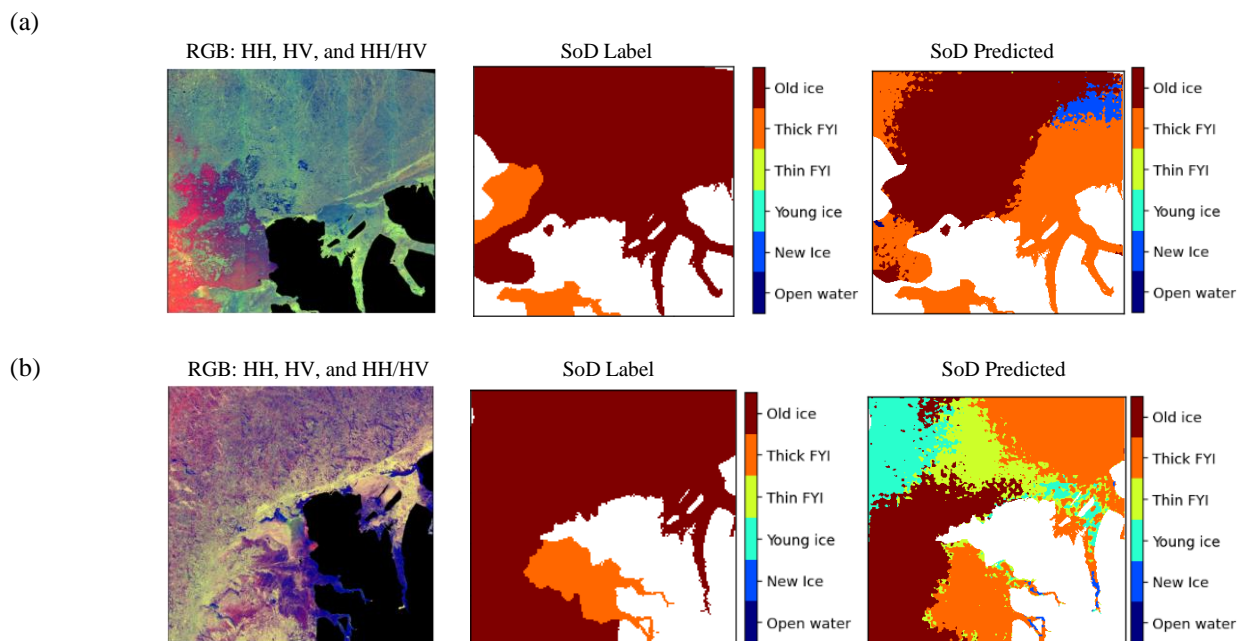


Fig. 18. False color image (RGB: HH, HV, and HH/HV) from (a) the “20210709T085811\_dmi\_prep” scene from the melting season and (b) “20210112T084156\_dmi\_prep” scene from the freezing season with the corresponding SoD labels and predicted charts.

SAR scenes from the test set in the melting (“20210709T085811\_dmi\_prep”) and freezing (“20210112T084156\_dmi\_prep”) seasons with the corresponding labels for SoD and predicted charts are shown in Fig. 18 (a) and (b), respectively. These scenes are selected to compare the classification of similar SoDs under melt and freeze conditions. In the predicted chart during the melting condition, differentiating between thick FYI and old ice is challenging, likely due to the presence of liquid water and melt ponds, which reduce microwave penetration and suppress volume scattering, leading to overlapping backscatter signatures. In the predicted chart in freezing condition, large number of old ice pixels are misclassified as young ice, thin FYI, and thick FYI, likely because surface scattering and the presence of brine-rich frost flowers at the snow-ice interface, which primarily affect FYI types in C-band SAR imagery (or the presence of mixed ice types), create overlapping signatures that make old ice appear similar to these FYI types, leading to misclassification.

## 5.5. Comparison with the State of the Art

### 5.5.1. Benchmark Test Performance Comparison

In this section, we compare the performance of our model to the state-of-the-art scores on the AutoICE benchmark dataset. MMSeaIce (X. Chen et al., 2024b), placed first in the AutoICE competition (Stokholm et al., 2024). Their model (MMSeaIce) utilized a U-Net architecture with four encoder-decoder blocks, where the first two blocks contained 32 filters, and the remaining blocks were configured with 64 filters. We implemented a U-Net model by replicating the architecture described in (X. Chen et al., 2024b) within our training pipeline to evaluate the effect of model architecture with other steps being equivalent (Table 6). In addition, we implemented another baseline U-Net model provided by Stokholm et al. (Stokholm et al., 2024) to AutoICE participants as a benchmark. We used the same validation set (1) and hyperparameters described in Section 4 to train these models. Data processing is the same for all models, meaning the difference in performance can be attributed to the model architecture.

Table 6 presents a summary comparison between the baselines and our model. Our model achieves higher validation scores for all tasks and test scores for combined score, SoD and FLOE tasks. Although our model architecture contains more parameters (46.12 M trainable parameters) than MMSeaIce model (U-Net: 1.03 M trainable parameters), it can be trained faster due to its reliance on the modern architecture of ResNet-152 backbone, whose bottleneck and skip connection structures allows for better flow of gradients and activations in the network. Given that the maximum epochs and patience were set to 120 and 80, respectively, all the models were trained for 120 epochs and saved based on the highest combined validation score.

Our model, X. Chen et al. (MMSeaIce) and Stokholm et al. (U-Net) models achieved the best combined validation score at epoch 63, 76 and 101, respectively. Our model architecture performs segmentations on lower-resolution feature maps (extracted by the ResNet-152 backbone) for operations, as stated in Section 4, followed by bilinear interpolation to scale the resulting segmentation maps to the original size, resulting in a speedup. In contrast, U-Net, processes larger dimension feature maps. U-Net has symmetric upsampling and downsampling components, and the feature concatenation at multiple levels, needing more convolution operations in the upsampling part, where it reconstructs the segmented image from high-level features.

MMSeaIce (X. Chen et al., 2024b) report a score of 87.3%, while our results indicate a combined score of 74.77% for our replication within our pipeline. This discrepancy can potentially be explained by the extra pre- and post-processing steps performed by (X. Chen et al., 2024b), including downsampling the dual-polarized SAR images, distance maps (DMs), and corresponding ice-charts, which according to their analysis, significantly improved their results, with combined scores metrics reported similar to ours. However, in this study, we are using the original scenes from the dataset for training and testing all models without further pre- and post-processing steps in an end-to-end set up. With this configuration, our model outperforms both U-Net baselines. Conceptually, the manual work of pre-processing the data to downsampling the input is similar to reducing the feature map dimensions by the ResNet-152 and DeepLabV3 architecture, and therefore, our model does not require the extra steps described in (X. Chen et al., 2024b) to achieve state-of-the-art performance, saving time and computational resources in both pre-processing as well as training steps. Similarly, our model outperforms Stokholm et al.'s model in SoD and FLOE tasks considerably, with slight underperformance in the SIC task. SAR scenes from the test set (20180707T113313\_cis\_prep scene) with the corresponding labels for SIC, SoD, and FLOE and predicted charts obtained from the baseline U-Net models: (a) X. Chen et al. (MMSeaIce), (b) Stokholm et al. (U-Net), and (c) our model (Customized DeepLabV3) are shown in Fig. 19. As shown in the predicted charts, the U-Net models particularly struggle with the correct prediction of thick FYI and big floe in SoD and FLOE tasks, respectively, and different percentage ratios of sea ice to open water in SIC chart.

**Table 6**

Comparison between the baseline U-Net models: X. Chen et al. (MMSeaIce), Stokholm et al. (U-Net), and our model (customized DeepLabV3). Note that the extra pre-processing steps described in (X. Chen et al., 2024b) are not performed. Models are tested within our end-to-end training pipeline, with every configuration except model architecture being the same.

Models	Validation				Test			
	Combined Score	SIC	SoD	FLOE	Combined Score	SIC	SoD	FLOE
<b>MMSeaIce</b> (X. Chen et al., 2024b)	84.66%	91.92%	80.79%	77.85%	74.77%	89.04%	66.76%	62.27%
<b>U-Net</b> (Stokholm et al., 2024)	87.98%	93.48%	86.60%	79.76%	79.33%	90.79%	74.71%	65.67%
<b>Ours</b>	92.56%	93.93%	94.55%	85.85%	86.90%	90.31%	89.79%	74.30%

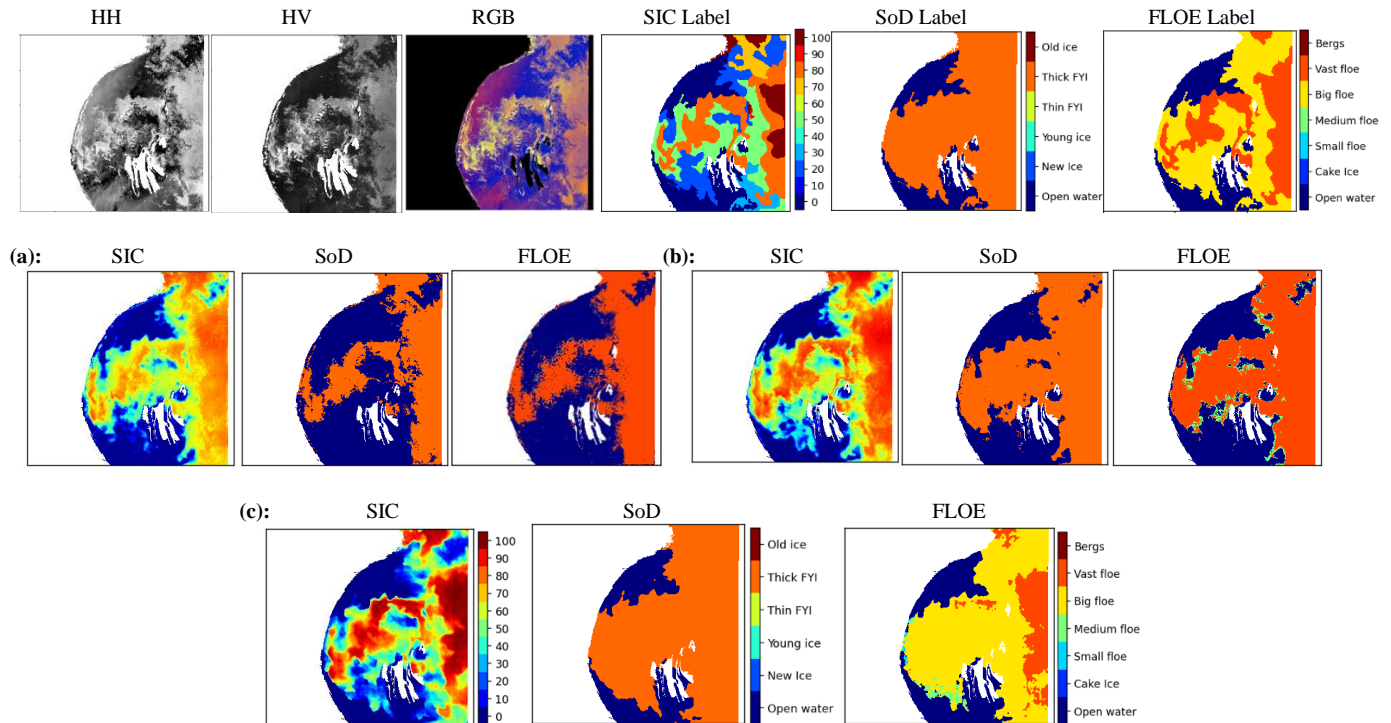


**Fig.19.** 20180707T113313\_cis\_prep scene from the test set with the corresponding labels for SIC, SoD, and FLOE and predicted charts obtained from the baseline U-Net models: (a) X. Chen et al. (MMSeaIce), (b) Stockholm et al. (U-Net), and (c) our model (Customized DeepLabV3).

### 5.5.2. Cross-Scene Generalization Comparison

Understanding the generalization capability of a model across different geographical regions is critical in operationalizing automated sea ice mapping. While geographic generalizability is a common issue given the small size of regional training datasets, our work above further highlighted that models that rely on location-specific features struggle even more when deployed in entirely different geographic regions, which can lead to reduced reliability in real-world applications.

To assess the cross-scene generalization capability of our approach, we compared its performance against the reported results of the Multimodal Fusion Domain Adaptive (MFDA) method proposed by (Y. Chen et al., 2024). They introduced this method to address the challenge of cross-scene retrieval of sea ice parameters, using the Canadian subset of the AutoICE benchmark, which contains 197 scenes as the source domain (training set, red squares) and the Greenland subset of 315 scenes as the target domain (test set, blue squares). Their approach incorporates normalized longitude and latitude data into their model, analogous to the relative position encoding within the transformer architecture, alongside HH and HV, AMSR2 (18.7 and 36.5 GHz), ERA5 variables (10 m wind speed, 2 m air temperature, total column water vapor, total column cloud liquid water), and time data (month of acquisition). In addition, we trained X. Chen et al. (MMSeaIce) and Stockholm et al. (U-Net) models on 197 Canadian scenes using their end-to-end training pipelines and data inputs and tested on 315 Greenland scenes to test geographic generalizability. MMSeaIce approach incorporates HH and HV, AMSR2 (18.7 and 36.5 GHz), ERA5 variables (10 m wind speed, 2 m air temperature, total column water vapor, total column cloud liquid water), latitude/longitude of each pixel and scene acquisition month. Stockholm et al. (U-Net) approach incorporates all the input channels in the dataset, excluding the latitude and longitude of subgrid points within the scene.

According to Table 7, MFDA and MMSeaIce approaches have considerably lower performance than our model. This is further indication that our approach more optimally relies on observation signals to learn more generalizable patterns across regions, without overfitting to location-specific information.

**Table 7**

Comparison between the MFDA (Y. Chen et al., 2024), MMSeaIce (X. Chen et al., 2024b), U-Net (Stokholm et al., 2024) and our model in cross-scene retrieval of sea ice parameters (Trained on 197 Canadian scenes and tested on 315 Greenland scenes).

Models	Test scores			
	SIC	SoD	FLOE	Combined Score
MFDA (Y. Chen et al., 2024)	78.0%	75.8%	79.8%	77.48%
MMSeaIce (X. Chen et al., 2024b)	81.847%	76.669%	80.554%	79.51%
U-Net (Stokholm et al., 2024)	90.148%	80.596%	87.301%	85.75%
<b>Ours</b>	93.328%	81.487%	86.628%	87.25%

## 6. Conclusion and future work

In this study, we enhanced the performance and efficiency of automating sea ice charting by developing a customized end-to-end DeepLabV3 model, which requires fewer training iterations and eliminates the need for additional pre- and post-processing stages in comparison to the current state of the art. We presented our pipeline and architecture, which simultaneously generates predictions for SIC, SoD, and FLOE in an end-to-end pipeline, achieving the state-of-the-art combined score of 87.3% on the AutoICE Challenge test set without the need for extra pre- or post-processing, and surpassing the current state-of-the-art for SoD by approximately 0.74 in F1 score. In addition, our approach outperforms state-of-the-art cross-scene sea ice retrieval, without incorporating longitude and latitude data into our model.

However, our interpretations, as summarized below, point to model memorization of regions and overfitting. Therefore, we believe that the score calculated on a model trained without geospatial encoding (i.e., location) is more indicative of real-world performance in other regions or under different climate conditions. As seen in Table 4, this means that the combined score of 81.82% (as a result of 89.89% for SIC, 78.19% for SoD, and 72.96% for FLOE) is a more reliable characterization of model performance in operational settings. This same conclusion applies for other models trained on the AutoICE challenge dataset, where the use of location as a feature may result in misleading high-scores. In other words, models using geospatial location as an input may inadvertently report inflated scores.

Our conclusions are based on interpretability modules including Gradient SHAP and Grad-CAM, as well as additional spatial cross-validation. We investigated the impact of incorporating location in the form of geospatial encoding for SIC estimation and classifying various targets in SoD and FLOE. Our results show that when testing on the benchmark-designated test set, geospatial encoding improves correct classification across all ice classes in SoD including new ice, young ice, thin FYI, thick FYI, and old ice. However, feature importance interpretation indicates model memorization of location and overfitting for specific ice types including thin FYI, regardless of observation signals, which would indicate problems for model generalizability to a different region not covered by the AutoICE dataset, or the same region under shifting climate conditions. In the case of FLOE, geospatial encodings appear to help for disambiguation of observations of big floe, and we do not observe concerning indications of model memorization and overfitting to different floe classes. However, FLOE scores are lower across the board compared to SIC and SoD.

Our spatial cross-validation set up also confirms that the scores previously reported on the AutoICE benchmark test set configuration are inflated due to the use of geospatial location in training and the test set designated for the Challenge. Our results indicate that incorporating geospatial encoding leads to model memorization and overfitting to the training regions which hurts the model's performance and generalizability when inference on different regions not covered by the dataset, and most likely even the same region under different climate conditions given that the model seems to rely heavily on location over remote sensed data for its predictions.

Our Gradient SHAP plot for SoD demonstrates that the HH channel has a positive contribution for classifying new and young ice due to its high sensitivity to surface scattering variations, and both HH and HV signals have high feature importance for classifying Thick FYI and Old ice. It also shows the relative importance of AMSR-2 variables at 18.7 and 36.5 GHz frequencies for classifying new ice, young ice, and thin FYI, indicating valuable features for mapping thin ice. On the other hand, our results validate that the contribution of HV channel in classifying most floe types is more than HH, which shows HV channel is more sensitive to floe size. Our findings also demonstrate that HH and HV signals are the most important features for predicting SIC, and then AMSR-2 at 18.7 (v) frequency provides the second most significant contribution.

This comprehensive analysis advances the development of automated sea ice mapping techniques and provides insights and guidance into how individual input features influence model performance and generalizability when using SAR and multi-source data. Our end-to-end architecture, spatial cross-validation and model interpretations also can be emulated in other remote sensing applications (e.g., land use and land cover mapping) to ensure model generalizability. Future research could incorporate additional data sources including L-band, X-band SAR or optical data to examine the performance and impact of individual features on the model's predictions for sea ice parameters. In the meanwhile, we tentatively accept automated sea ice charting will result in lower than ideal performance that is not ready for operational scenarios. Focus can be placed on identifying uncertain regions in model predictions where human quality control can improve model output. An evaluation of the models' uncertainty across different tasks using multi-source data and different fusion techniques would be worthwhile for various operational and scientific applications. Developing further spatial cross-validation techniques that incorporate both within- and inter-region metrics can further facilitate model development with more reliability for deployment in the field.

### CRediT authorship contribution statement

**Sepideh Jalayer:** Writing – original draft, Writing – review & editing, Visualization, Software, Methodology, Formal analysis, Conceptualization, Validation. **Samira Alkaee Taleghan:** Review & editing, Software, Methodology. **Rafael Pires de Lima:** Review & editing, Methodology. **Behzad Vahedi:** Review & editing, Methodology. **Nick Hughes:** Review & editing, Conceptualization. **Farnoush Banaei-Kashani:** Review & editing, Conceptualization. **Morteza Karimzadeh:** Investigation, Writing – original draft, Writing – review & editing, Supervision, Project administration, Methodology, Conceptualization, Funding acquisition.

### Acknowledgments

This work was supported by the U.S. National Science Foundation under Grant 2026962 and Grant 2026865.

### Data availability

In this study, we used the publicly available dataset from the AutoICE Challenge (Stokholm et al., 2024), and our code is available at: <https://github.com/geohai/autoice-challenge-geospatial-encoding>.

### References

- Andersson, T.R., Hosking, J.S., Pérez-Ortiz, M., Paige, B., Elliott, A., Russell, C., Law, S., Jones, D.C., Wilkinson, J., Phillips, T., Byrne, J., Tietsche, S., Sarojini, B.B., Blanchard-Wrigglesworth, E., Aksenov, Y., Downie, R., Shuckburgh, E., 2021. Seasonal Arctic sea ice forecasting with probabilistic deep learning. *Nat Commun* 12. <https://doi.org/10.1038/s41467-021-25257-4>
- Barber, D.G., Hanesiak, J.M., Yackel, J.J., 2001. Sea ice, radarsat-1 and arctic climate processes: A review and update. *Canadian Journal of Remote Sensing* 27, 51–61. <https://doi.org/10.1080/07038992.2001.10854919>
- Boulze, H., Korosov, A., Brajard, J., 2020. Classification of sea ice types in sentinel-1 SAR data using convolutional neural networks. *Remote Sens (Basel)* 12. <https://doi.org/10.3390/rs12132165>
- Buus-Hinkler, J.W.T.S.A.R.K.A.S.R.P.L.T. et al. (2022). A.S.I.C.Dataset.T.U. of Denmark.Collection. <https://doi.org/10.11583/DTU.c.6244065.v2>, n.d. collection\_6244065\_v2\_citations. <https://github.com/astokholm/AI4ArcticSeaIceChallenge>.
- Chen, Liang-Chieh & Papandreou, George & Schroff, Florian & Adam, Hartwig. (2017). Rethinking Atrous Convolution for Semantic Image Segmentation. 10.48550/arXiv.1706.05587.
- Chen, X., Cantu, F.J.P., Patel, M., Xu, L., Brubacher, N.C., Scott, K.A., Clausi, D.A., 2024a. A comparative study of data input selection for deep learning-based automated sea ice mapping. *International Journal of Applied Earth Observation and Geoinformation* 131. <https://doi.org/10.1016/j.jag.2024.103920>
- Chen, X., Patel, M., Pena Cantu, F.J., Park, J., Turnes, J.N., Xu, L., Scott, K.A., Clausi, D.A., 2024b. MMSeaIce: a collection of techniques for improving sea ice mapping with a multi-task model. *Cryosphere* 18, 1621–1632. <https://doi.org/10.5194/tc-18-1621-2024>
- Chen, X., Patel, M., Xu, L., Chen, Y., Scott, K.A., Clausi, D.A., 2024c. Weakly Supervised Learning for Pixel-Level Sea Ice Concentration Extraction Using AI4Arctic Sea Ice Challenge Dataset. *IEEE Geoscience and Remote Sensing Letters* 21, 1–5. <https://doi.org/10.1109/LGRS.2023.3338061>

- Chen, Y., Yan, Q., Bashmachnikov, I., Huang, K., Mu, F., Zhang, Z., Xu, M., Zhao, J., 2024. MFDA: Unified Multi-Task Architecture for Cross-Scene Sea Ice Classification. *IEEE Transactions on Geoscience and Remote Sensing*. <https://doi.org/10.1109/TGRS.2024.3491190>
- De Gelis, I., Colin, A., Longepe, N., 2021. Prediction of Categorized Sea Ice Concentration from Sentinel-1 SAR Images Based on a Fully Convolutional Network. *IEEE J Sel Top Appl Earth Obs Remote Sens* 14, 5831–5841. <https://doi.org/10.1109/JSTARS.2021.3074068>
- Dierking, W., 2013. Sea Ice Monitoring by Synthetic Aperture Radar. *Oceanography* 26. <https://doi.org/10.5670/oceanog.2013.33>
- Dierking, W., 2010. Mapping of different sea ice regimes using images from sentinel-1 and ALOS synthetic aperture radar. *IEEE Transactions on Geoscience and Remote Sensing* 48, 1045–1058. <https://doi.org/10.1109/TGRS.2009.2031806>
- Færch, L., Dierking, W., Hughes, N., Doulgeris, A.P., 2024. Mapping icebergs in sea ice: An analysis of seasonal SAR backscatter at C- and L-band. *Remote Sens Environ* 304. <https://doi.org/10.1016/j.rse.2024.114074>
- Gibson, G., Weijer, W., Jeffery, N., Wang, S., 2020. Relative Impact of Sea Ice and Temperature Changes on Arctic Marine Production. *J Geophys Res Biogeosci* 125. <https://doi.org/10.1029/2019JG005343>
- Guo, W., Itkin, P., Lohse, J., Johansson, M., Doulgeris, A.P., 2022. Cross-platform classification of level and deformed sea ice considering per-class incident angle dependency of backscatter intensity. *Cryosphere* 16, 237–257. <https://doi.org/10.5194/tc-16-237-2022>
- Guo, X., Hou, B., Wu, Z., Ren, B., Wang, S., Jiao, L., 2022. Prob-POS: A Framework for Improving Visual Explanations from Convolutional Neural Networks for Remote Sensing Image Classification. *Remote Sens (Basel)* 14. <https://doi.org/10.3390/rs14133042>
- Hacıfendioglu, K., Başağa, H.B., Yavuz, Z., Karimi, M.T., 2022. Intelligent ice detection on wind turbine blades using semantic segmentation and class activation map approaches based on deep learning method. *Renew Energy* 182, 1–16. <https://doi.org/10.1016/j.renene.2021.10.025>
- Huang, R., Wang, C., Li, J., Sui, Y., 2023. DF-UHRNet: A Modified CNN-Based Deep Learning Method for Automatic Sea Ice Classification from Sentinel-1A/B SAR Images. *Remote Sens (Basel)* 15. <https://doi.org/10.3390/rs15092448>
- Huang, W., Yu, A., Xu, Q., Sun, Q., Guo, W., Ji, S., Wen, B., Qiu, C., 2024. Sea Ice Extraction via Remote Sensing Imagery: Algorithms, Datasets, Applications and Challenges. *Remote Sens (Basel)*. <https://doi.org/10.3390/rs16050842>
- Huang, Y., Ren, Y., Li, X., 2024. Deep learning techniques for enhanced sea-ice types classification in the Beaufort Sea via SAR imagery. *Remote Sens Environ* 308. <https://doi.org/10.1016/j.rse.2024.114204>
- Isleifson, D., Galley, R.J., Firoozy, N., Landy, J.C., Barber, D.G., 2018. Investigations into frost flower physical characteristics and the C-band scattering response. *Remote Sens (Basel)* 10. <https://doi.org/10.3390/rs10070991>
- Kawauchi, H., Fuse, T., 2022. SHAP-Based Interpretable Object Detection Method for Satellite Imagery. *Remote Sens (Basel)* 14. <https://doi.org/10.3390/rs14091970>
- Key, J.R., Schweiger, Axel, Key, J., Maslanik, J A, Schweiger, A ], 2014. Classification of merged AVHRR and SMMR Arctic data with neural networks.
- Khaleghian, S., Ullah, H., Kræmer, T., Hughes, N., Eltoft, T., Marinoni, A., 2021. Sea ice classification of sar imagery based on convolution neural networks. *Remote Sens (Basel)* 13. <https://doi.org/10.3390/rs13091734>
- Liu, H., Guo, H., Zhang, L., 2015. SVM-Based Sea Ice Classification Using Textural Features and Concentration From RADARSAT-2 Dual-Pol ScanSAR Data. *IEEE J Sel Top Appl Earth Obs Remote Sens* 8, 1601–1613. <https://doi.org/10.1109/JSTARS.2014.2365215>
- Liu, P., Biljecki, F., 2022. A review of spatially-explicit GeoAI applications in Urban Geography. *International Journal of Applied Earth Observation and Geoinformation* 112. <https://doi.org/10.1016/j.jag.2022.102936>
- Lundberg, Scott & Lee, Su-In. (2017). A Unified Approach to Interpreting Model Predictions. 10.48550/arXiv.1705.07874.
- Lyu, H., Huang, W., Mahdianpari, M., 2022. A Meta-Analysis of Sea Ice Monitoring Using Spaceborne Polarimetric SAR: Advances in the Last Decade. *IEEE J Sel Top Appl Earth Obs Remote Sens* 15, 6158–6179. <https://doi.org/10.1109/JSTARS.2022.3194324>
- Mac Aodha, O., Cole, E., Perona, P., 2019. Presence-Only Geographical Priors for Fine-Grained Image Classification.
- Mai, G., Janowicz, K., Hu, Y., Gao, S., Yan, B., Zhu, R., Cai, L., Lao, N., 2022. A review of location encoding for GeoAI: methods and applications. *International Journal of Geographical Information Science*. <https://doi.org/10.1080/13658816.2021.2004602>
- Makynen, M., Simila, M., 2022. AMSR2 Thin Ice Detection Algorithm for the Arctic Winter Conditions. *IEEE Transactions on Geoscience and Remote Sensing* 60. <https://doi.org/10.1109/TGRS.2022.3142966>
- Meier, W.N., Hovelsrud, G.K., Van Oort, B.E.H., Key, J.R., Kovacs, K.M., Michel, C., Haas, C., Granskog, M.A., Gerland, S., Perovich, D.K., Makshtas, A., Reist, J.D., 2014. Arctic sea ice in transformation: A review of recent observed changes and impacts on biology and human activity. *Reviews of Geophysics*. <https://doi.org/10.1002/2013RG000431>
- Nakata, K., Ohshima, K.I., Nishihashi, S., 2019. Estimation of Thin-Ice Thickness and Discrimination of Ice Type from AMSR-E Passive Microwave Data. *IEEE Transactions on Geoscience and Remote Sensing* 57, 263–276. <https://doi.org/10.1109/TGRS.2018.2853590>
- Onstott, R.G., 2011. SAR and scatterometer signatures of sea ice. pp. 73–104. <https://doi.org/10.1029/gm068p0073>

- Partington, K.C., Flach, J.D., Barber, D., Isleifson, D., Meadows, P.J., Verlaan, P., 2010. Dual-polarization C-band radar observations of sea ice in the amundsen gulf. *IEEE Transactions on Geoscience and Remote Sensing* 48, 2685–2691. <https://doi.org/10.1109/TGRS.2009.2039577>
- Pires De Lima, R., Karimzadeh, M., 2023. Model Ensemble With Dropout for Uncertainty Estimation in Sea Ice Segmentation Using Sentinel-1 SAR. *IEEE Transactions on Geoscience and Remote Sensing* 61, 1–15. <https://doi.org/10.1109/TGRS.2023.3331276>
- Pires de Lima, R., Vahedi, B., Hughes, N., Barrett, A.P., Meier, W., Karimzadeh, M., 2023. Enhancing sea ice segmentation in Sentinel-1 images with atrous convolutions. *Int J Remote Sens* 44, 5344–5374. <https://doi.org/10.1080/01431161.2023.2248560>
- Qu, M., Lei, R., Liu, Y., Li, N., 2024. Arctic Sea ice leads detected using sentinel-1B SAR image and their responses to atmosphere circulation and sea ice dynamics. *Remote Sens Environ* 308. <https://doi.org/10.1016/j.rse.2024.114193>
- Rußwurm, M., Klemmer, K., Rolf, E., Zbinden, R., & Tuia, D. (2023). Geographic location encoding with spherical harmonics and sinusoidal representation networks. *Proceedings of the International Conference on Learning Representations (ICLR)*.
- Scott, K.A., Buehner, M., Carrieres, T., 2014. An assessment of sea-ice thickness along the Labrador coast from AMSR-E and MODIS data for operational data assimilation. *IEEE Transactions on Geoscience and Remote Sensing* 52, 2726–2737. <https://doi.org/10.1109/TGRS.2013.2265091>
- Selvaraju, R.R., Cogswell, M., Das, A., Vedantam, R., Parikh, D., Batra, D., 2017. Grad-CAM: Visual Explanations from Deep Networks via Gradient-Based Localization, in: *Proceedings of the IEEE International Conference on Computer Vision*. Institute of Electrical and Electronics Engineers Inc., pp. 618–626. <https://doi.org/10.1109/ICCV.2017.74>
- Shokr, M., Dabboor, M., 2023. Polarimetric SAR Applications of Sea Ice: A Review. *IEEE J Sel Top Appl Earth Obs Remote Sens* 16, 6627–6641. <https://doi.org/10.1109/JSTARS.2023.3295735>
- Smilkov, D., Thorat, N., Kim, B., Viégas, F., Wattenberg, M., 2017. SmoothGrad: removing noise by adding noise.
- Song, W., Li, M., Gao, W., Huang, D., Ma, Z., Liotta, A., Perra, C., 2021. Automatic Sea-Ice Classification of SAR Images Based on Spatial and Temporal Features Learning. *IEEE Transactions on Geoscience and Remote Sensing* 59, 9887–9901. <https://doi.org/10.1109/TGRS.2020.3049031>
- Stokholm, A., Buus-Hinkler, J., Wulf, T., Korosov, A., Saldo, R., Pedersen, L.T., Arthurs, D., Dragan, I., Modica, I., Pedro, J., Debień, A., Chen, X., Patel, M., Cantu, F.J.P., Turnes, J.N., Park, J., Xu, L., Scott, K.A., Clausi, D.A., Fang, Y., Jiang, M., Taleghanidoozdoozan, S., Brubacher, N.C., Soleymani, A., Gousseau, Z., Smaczny, M., Kowalski, P., Komorowski, J., Rijlaarsdam, D., van Rijn, J.N., Jakobsen, J., Rogers, M.S.J., Hughes, N., Zagon, T., Solberg, R., Longépé, N., Kreiner, M.B., 2024. The AutoICE Challenge. *Cryosphere* 18, 3471–3494. <https://doi.org/10.5194/tc-18-3471-2024>
- Stokholm, A., Wulf, T., Kucik, A., Saldo, R., Buus-Hinkler, J., Hvidegaard, S.M., 2022. AI4SeaIce: Toward Solving Ambiguous SAR Textures in Convolutional Neural Networks for Automatic Sea Ice Concentration Charting. *IEEE Transactions on Geoscience and Remote Sensing* 60. <https://doi.org/10.1109/TGRS.2022.3149323>
- Sundararajan, M., Taly, A., Yan, Q., 2017. Axiomatic Attribution for Deep Networks.
- Tavri, A., Scharien, R., Geldsetzer, T., 2023. Melt Season Arctic Sea Ice Type Separability Using Fully and Compact Polarimetric C- and L-Band Synthetic Aperture Radar. *Canadian Journal of Remote Sensing* 49. <https://doi.org/10.1080/07038992.2023.2271578>
- Toyota, T., Ishiyama, J., Kimura, N., 2021. Measuring Deformed Sea Ice in Seasonal Ice Zones Using L-Band SAR Images. *IEEE Transactions on Geoscience and Remote Sensing* 59, 9361–9381. <https://doi.org/10.1109/TGRS.2020.3043335>
- Vahedi, B., Lucas, B., Banaei-Kashani, F., Barrett, A.P., Meier, W.N., Khalsa, S.J., Karimzadeh, M., 2024. Partial Label Learning with Focal Loss for Sea Ice Classification Based on Ice Charts. *IEEE J Sel Top Appl Earth Obs Remote Sens*. <https://doi.org/10.1109/JSTARS.2024.3413003>
- Wagner, P.M., Hughes, N., Bourbonnais, P., Stroeve, J., Rabenstein, L., Bhatt, U., Little, J., Wiggins, H., Fleming, A., 2020. Sea-ice information and forecast needs for industry maritime stakeholders. *Polar Geography* 43, 160–187. <https://doi.org/10.1080/1088937X.2020.1766592>
- Wang, Y.R., Li, X.M., 2021. Arctic sea ice cover data from spaceborne synthetic aperture radar by deep learning. *Earth Syst Sci Data* 13, 2723–2742. <https://doi.org/10.5194/essd-13-2723-2021>
- Yan, Q., Huang, W., 2016. Spaceborne GNSS-R Sea Ice Detection Using Delay-Doppler Maps: First Results from the U.K. TechDemoSat-1 Mission. *IEEE J Sel Top Appl Earth Obs Remote Sens* 9, 4795–4801. <https://doi.org/10.1109/JSTARS.2016.2582690>
- Ye, Y., Luo, Y., Sun, Y., Shokr, M., Aaboe, S., Girard-Ardhuin, F., Hui, F., Cheng, X., Chen, Z., 2023. Inter-comparison and evaluation of Arctic sea ice type products. *Cryosphere* 17, 279–308. <https://doi.org/10.5194/tc-17-279-2023>
- Zabolotskikh, E., Azarov, S., 2022. Wintertime Emissivities of the Arctic Sea Ice Types at the AMSR2 Frequencies. *Remote Sens (Basel)* 14. <https://doi.org/10.3390/rs14235927>
- Zakhvatkina, N., Korosov, A., Muckenhuber, S., Sandven, S., Babiker, M., 2017. Operational algorithm for ice-water classification on dual-polarized RADARSAT-2 images. *Cryosphere* 11, 33–46. <https://doi.org/10.5194/tc-11-33-2017>
- Zakhvatkina, N., Smirnov, V., Bychkova, I., 2019. Satellite SAR data-based sea ice classification: An overview. *Geosciences (Switzerland)*. <https://doi.org/10.3390/geosciences9040152>

Zhang, Y., Zhu, T., Spreen, G., Melsheimer, C., Huntemann, M., Hughes, N., Zhang, S., Li, F., n.d. Sea ice and water classification on dual-polarized Sentinel-1 imagery during melting season. <https://doi.org/10.5194/tc-2021-85>

Zhao, L., Xie, T., Perrie, W., Yang, J., 2024. Sea Ice Detection from RADARSAT-2 Quad-Polarization SAR Imagery Based on Co- and Cross-Polarization Ratio. *Remote Sens (Basel)* 16. <https://doi.org/10.3390/rs16030515>

Zhu, Y., Tao, T., Li, J., Yu, K., Wang, L., Qu, X., Li, S., Semmling, M., Wickert, J., 2021. Spaceborne gnss-r for sea ice classification using machine learning classifiers. *Remote Sens (Basel)* 13. <https://doi.org/10.3390/rs13224577>